

Airborne Scatterometers: Investigating Ocean Backscatter Under Low- and High-Wind Conditions

J.R. Carswell¹, S.C. Carson², R.E. McIntosh³, F.K. Li⁴, G. Neumann⁵,
D.J. McLaughlin⁶, J.C. Wilkerson⁷, P.G. Black⁸

¹**Microwave** Remote Sensing Laboratory, University of Massachusetts, Amherst, MA 01003, Tel: (413)545-0779,
Fax: (413)545-4652, Email: carswell@alex.ecs.umass.edu (Contact Author)

²**RCOPower** Technologies Inc., Apt. 1, 1250 24th Street NW, Washington D.C. 20009, Tel: (202)223-8808,
Fax: (202)223-1377, Email: scarson@access.digex.net

³**Microwave** Remote Sensing Laboratory, University of Massachusetts, Amherst, MA 01003, Tel: (413)545-0779,
Fax: (413)545-4652, Email: mcintosh@alex.ecs.umass.edu

⁴Jet Propulsion Laboratory, California Institute of Technology, 4800 Oak Grove Drive, M/S 300-227, Pasadena,
CA 91109, Tel: (818)354-2849, Fax: (818)393-5285, Email: fuk li@radar-email.jpl.nasa.gov

⁵Jet Propulsion Laboratory, California Institute of Technology, 4800 Oak Grove Drive, M/S 300-319, Pasadena,
CA 91109, Tel: (818)354-7273, Fax: (818)393-5285, Email: gregory.neumann@ccmail.jpl.nasa.gov

⁶Electrical and Computer Engineering, Northeastern University, Boston, MA 02115, Tel: (617)373-2032, Fax:
(617)437-8627, Email: mclaughlin@bode.cdsp.neu.edu

⁷National Environmental Satellite, Data and Information Service, National Oceanic and Atmospheric Adminis-
tration, Washington, D.C. 20233, Tel: (301)763-8231, Fax: (301)763-8108, Omnet: j.wilkerson

⁸**Hurricane** Research Laboratory, National Oceanic and Atmospheric Administration, Coral Gables, Florida
33145, Tel: (305)361-4320, Email: black@guust1.aoml.erl.gov

ABSTRACT

Attempting to understand and predict weather on a local and global basis has challenged both the scientific and engineering communities. One key parameter in understanding the weather is the ocean surface wind vector because of its role in the energy exchange at the air-sea interface. Scatterometers, radars that measure the reflectivity of a target, offer a tool in which to remotely monitor these winds from tower, aircraft and satellite-based platforms. This paper introduces three current airborne scatterometer systems, and presents data collected by these instruments under low-, moderate- and high-wind conditions. Our paper focuses on airborne scatterometers because of their ability to resolve submesoscale variations in wind fields. Discrepancies between existing theory and the observations are noted and concerns in measuring low-wind speeds discussed. Finally the application of using this technology for estimating the surface wind vector during a hurricane is demonstrated.

1. INTRODUCTION

Predicting the weather and understanding climatology on a global basis has challenged the scientific and engineering disciplines, though the benefits of meeting these challenges are tremendous: daily forecasting, early warnings of severe storms, understanding long-term patterns such as droughts and determining the effects we have on the climate. To accomplish these and other weather-related tasks, knowledge of the interaction between the ocean and the atmosphere is essential. The near surface wind is the key parameter coupling the ocean and the atmosphere, so global monitoring of this wind is therefore crucial. Scatterometer technology is now making this goal achievable. In this paper we focus on airborne scatterometers because of their ability to resolve submesoscale variations in wind fields.

A scatterometer [1] [2] is a radar that measures the absolute reflectivity or radar cross section [3] of a target by transmitting a known amount of power at it and measuring the power it reflects back. This return power is related to the radar parameters and radar cross section of a surface target by [4]

$$P_r = \int_{A_{ill}} \frac{P_t G^2 \lambda^2 \sigma_o}{(4\pi)^3 R^4} dA \quad (1)$$

where:

A_{ill} = Area illuminated

P_r = Received power

P_t = Transmit power

G = Antenna gain pattern

λ = Radar wavelength

R = Distance to surface

σ_o = Normalized radar cross section

In this equation the radar cross section is normalized to the area illuminated. Typically for surface targets such as the ocean that encompass the entire footprint, values are reported in terms of the normalized radar cross section, NRCS, rather than the radar cross section. This removes the dependence on the size of footprint. Assuming that the NRCS and P_t

arc constant over the footprint, the measured NRCS is expressed as

$$\sigma^0 = \frac{(4\pi)^3 P_r}{P_t \lambda^2 \int_{A_{ill}} \frac{G^2}{R^4} dA} \quad (2)$$

To accurately measure this quantity, the antenna gain and pattern, the power transmitted, the system gains, and the distance to the surface must be known. Through external calibrations the antenna parameters can be measured; while sampling the transmit power and thermal noise of the system (internal calibration) allows monitoring of the transmit power and system gains [5]. With this knowledge, the NRCS can be calculated from the receive power measurements.

Furthermore, at microwave frequencies, the NRCS of the ocean surface is related to the spectral density of the capillary-gravity waves. The growth of these waves is strongly correlated with the surface winds; thus these winds can be inferred using a scatterometer [1]. Unfortunately, the exact relationship between the radar cross section and the ocean surface winds is still not known [6]. Current systems rely on empirical models derived from data collected using satellite, airborne and tower-based scatterometers. This paper focuses on airborne systems and their unique capability to observe backscatter measurements on a sub-mesoscale basis. Understanding the wind dependence of these backscatter measurements has direct implications on using scatterometers to estimate the near surface wind vector for which the wind field exhibits strong spatial variability such as the low-wind regions near the equator or exhibits steep spatial gradients such as in hurricanes.

This paper outlines the general history and theory of scatterometry and presents three airborne scatterometer systems currently being used to investigate the relationship between the NRCS of the ocean surface under low- and high-wind conditions. Section II describes the three scatterometer systems: a dual polarized Ku-band airborne scatterometer, a C-band airborne scatterometer, and a combined C/Ku-band airborne scatterometer. Section III presents data collected by these instruments, and Section IV discusses the implications of the data and the future direction of scatterometry.

A. History

Scattering from the ocean surface has been studied since the end of the Second World War, when the Navy, interested in detecting targets on the surface of the ocean, launched

an effort to study the radar echo from the ocean [7]. At first the ocean was viewed as clutter, but by the early 1950s observations indicated that the off-nadir NRCS of the ocean at microwave frequencies was influenced by the surface winds.

Through 1950s and 1960s, several experiments were performed to investigate the wind dependence of the NRCS, and to determine if this relationship could be used as a tool to estimate the surface winds. The United States Naval Research Laboratory (NRL), using multifrequency radars, was actively involved in several airborne and platform experiments [8]-[11]. Observations collected showed a strong wind dependence but calibration errors led to the misconception that a saturation occurred at $6 \text{ m}\cdot\text{s}^{-1}$. Along with NRL, the National Aeronautics Space Agency Johnson Space Center (NASA-JSC) conducted an extensive set of airborne experiments using a 13.3 GHz fan beam scatterometer [12]. Again due to poor calibrations, biases existed from experiment to experiment, but once these were removed, the data collected showed increasing NRCS values with increasing winds [1][13].

By the seventies, satellite base experiments were performed on SKYLAB which was launched with a combined radiometer/scatterometer system, S-193 RADSCAT, on board. Its purpose was to validate the concept of using a spaceborne radiometer/scatterometer as a tool to measure the surface winds above the ocean[14]; the radiometer would measure atmospheric attenuation and the 13.3 GHz scatterometer would measure the NRCS of the ocean surface. The atmospheric attenuation measurements were necessary to correct for the propagation loss suffered by the transmitted pulse from the scatterometer[15]. During its operation in 1973 and 1974, S-193 collected relatively large data sets compared to previous airborne missions. These measurements indicated that the NRCS was correlated with the wind speed and suggested a power law relationship for incidence angles ranging from 30° to 50° [15][16].

In conjunction with S-193 RADSCAT, a similar instrument, the Advanced Applications Flight Experiments radiometer/scatterometer (AAFERADSCAT) was developed and installed on the NASA-JSC C-130 [17]. A set of flight known as the circle flights were flown to determine the azimuthal dependence of the NRCS relative to the wind direction. These important missions consisted of flying the aircraft in 360° turns at a constant bank angle chosen so that the AAFERADSCAT look direction was at a fixed incidence angle between

0° and 50°. These measurements clearly documented the dependence of NRCS on wind direction; a three term fourier cosine series model was developed [18] -[20].

The next development was NASA's SeaSat-A Satellite Scatterometer (SASS) which took advantage of the knowledge gained from the AAFB RADSCAT program, SKYLAB, and previous scatterometers. Unlike its predecessor, S-1 93, SASS design incorporated four fan beam antennas to provide information about the anisotropy of the NRCS with respect to the wind direction [21]. An advantage of this configuration was that it provided two different azimuthal looks at each resolution cell making it was possible to estimate the surface wind direction as well as the speed. Some ambiguities existed in the wind estimate since more than two azimuthal looks were needed to fully sample the anisotropy of the NRCS, nonetheless SASS effectively measured the surface wind vector on a global basis [22]- [26].

Since then, several airborne and platform-based scatterometers have obtained backscatter measurements[27]- [37]. Recently, the European Space Agency launched the ERS-1 satellite with the AMI scatterometer on board. This 5.3 GHz scatterometer has three vertically polarized antennas pointing at 45°, 90°, and 135° relative to the satellite track and is providing a wealth of C-Band NRCS measurements. These measurements are being used to provide global wind estimates using the CMOD4 empirical model function [38]. Comparisons of these wind estimates with NMC predicted winds show they are within approximately $2 \text{ m} \cdot \text{s}^{-1}$ for winds between $4 \text{ m} \cdot \text{s}^{-1}$ to $12 \text{ m} \cdot \text{s}^{-1}$ [39]. In 1996 this scatterometer will be joined with the NASA Ku-band scatterometer, NSCAT[40] which will reside on the Japan. National Space Agency's (NASDA) Advanced Earth Observing Satellite (ADEOS). The combination of the AMI scatterometer and NSCAT will provide global surface wind vector estimates for almost all weather patterns.

B. Theory

The physics of off-nadir microwave backscatter from the ocean surface are not completely understood. The first attempts to develop theoretical models to predict the backscatter from the ocean were in the 1950s, when investigators applied physical optics or Kirchoff approximation to the ocean surface. However, this often underestimated the radar echo and could not explain the weaker returns for horizontal polarization compared to vertical

[1][7][41]. It wasn't until 1968 that Wright [42] and Bass [43] independently derived a theoretical model known as the composite surface model. This theory was an extension of the technique applied by Rice [44] to explain the radar return from a slightly rough surface. By treating the ocean as a collection of facets, each with a slight perturbation in its roughness and individually tilted by the larger gravity waves, the criteria of first order perturbation theory was satisfied and first order perturbation applied. The result is that the NRCS is given as

$$\sigma_{facet}^{\circ} = 16\pi k_o^4 |g_{pp}(\theta_o)|^2 \psi(0, 2k_o \sin \theta_o) \quad (3)$$

where ψ is the two dimensional surface roughness spectrum and g_{pp} is the modified Fresnel reflection coefficient. The subscripts, pp, represent the transmit and receive polarizations. (Plant goes through a detailed derivation.) [41]

Since each facet was assumed to be independent of the next, the total NRCS is the summation of the cross section of each facet weighted by the slope probability of the long waves, $P(\alpha, \phi)$ [45], and normalized by the area illuminated. It is given by

$$\sigma^{\circ} = 16\pi k_o^4 \int |g_{pp}(\theta, \alpha, \phi)|^2 \psi(2k_o \cos \theta_o, 2k_o \sin \theta') P(\alpha, \phi) d\alpha d\phi \quad (4)$$

where α and ϕ are the tilt angles induced by the long waves on the facet and $\theta' = \theta_o - \alpha$.

Composite surface theory seems to describe well the microwave backscatter at intermediate incidence angles from the ocean surface. (See Moore and Fung, 1979 [1] and Valenzuela, 1978 [46] for a review). It accounts for previous discrepancies such as the difference in σ° for horizontal and vertical polarization. The theory also provides a physical explanation for the observed wind dependence based on the surface roughness spectrum (wave spectra), ψ . That is, composite surface theory states that σ° is proportional to the mean spectral density of the Bragg resonant capillary-gravity wave on the ocean surface,. These waves are dependent on the local surface winds, thereby implying that σ° depends on the local wind.

Current composite surface based models have been proposed by Donelan and Pierson [47], Plant [48], and Durden and Vesccky [49]. Each models the full wave spectra slightly different; none of them share full success in predicting the NRCS for all surface conditions, and all underestimate the NRCS for horizontal polarization. A different approach is now

being investigated called the integral equation method. This technique seeks an approximate solution for the electromagnetic surface currents through iterative solutions of the integral equation. These currents are then used to calculate the scattered far fields [50]. Recently, Chen et al. have applied non-Gaussian statistics to model the surface radar cross section and used this integral equation method [51]. Their results show good agreement with both vertical and horizontal polarized measurements, but only a limited number of observations are compared. More work is needed to verify this technique over a variety of wind and surface conditions.

Failure of theoretical models to correctly predict σ° for a variety of sea and atmospheric conditions has led to the continual development of empirical models. Two presently used models are SASS-II for Ku-band [52] and CMOD4 for C-band [38]. SASS-II model function was derived using 3 months of data from SASS. It assumes a bivariate normal probability function to represent the probability distribution function of the global ocean wind speed to derive a model function that maps these assumed statistics of the wind to the SASS σ° statistics. The basic form of the model is

$$u'' = A_0 + A_1 \cos \phi + A_2 \cos 2\phi \quad (5)$$

and

$$A_0 = a_0 U^{\alpha_0}$$

$$A_1 = (a_1 + \alpha_1 \log U) A_0$$

$$A_2 = (a_2 + \alpha_2 \log U) A_0$$

where ϕ is the azimuthal angle relative to the upwind direction, and the coefficients $a_0, a_1, a_2, \alpha_0, \alpha_1$, and α_2 are fit parameters that are dependent on incidence angle and polarization.

The CMOD4 empirical model function was derived using data obtained from the AMI scatterometer on the ERS-1 satellite, in-situ wind measurements, and wind vector predictions from the European Center of Medium-Range Weather Forecasting (ECMWF) model. The functional form of this model is

$$\sigma_o = b_0 (1 + b_1 \cos \phi + b_2 \tanh b_3 \cos 2\phi)^{1.6} \quad (6)$$

and

$$b_0 = \delta \times 10^{\alpha + \gamma \cdot F(U + \beta)}$$

$$F(y) = \begin{cases} 6 & \text{if } y \leq 0 \\ \log_{10} z_1(y) & \text{if } 0 \leq y \leq 5 \\ \frac{\sqrt{y}}{3.2} & \text{if } y > 5 \end{cases}$$

where ϕ is the azimuth angle relative to the upwind direction, δ is a incidence angle bias correction, and $\alpha, \beta, \gamma, b_1, b_2$, and b_3 are empirically determined coefficients expressed as combinations of Legendre polynomials.

These two models describe observations under moderate wind conditions fairly well. However, at low and high wind speeds, their predictions significantly depart from observations. Additional measurements are needed for further modifications of these models. The combination of satellite data from ERS-1 and NSCAT and high resolution data from airborne and platform-based scatterometers will provide these measurements.

11. INSTRUMENT DESCRIPTIONS

Three high resolution airborne scatterometers presently being used to investigate discrepancies between observations and theoretical models are the Jet Propulsion Laboratory (JPL) Ku-band scatterometer, NUSCAT; University of Massachusetts (UMASS) C-band Scatterometer, C-SCAT; and UMASS C/Ku-band scatterometer, C-SCATII/KU-SCAT. A description of each instrument follows.

A. NUSCAT

NUSCAT is a Ku-band pulsed scatterometer developed by JPL. This radar consists of 4 subsections: RF front end, antenna, data acquisition, and controller. Figure 1 shows a general block diagram. The RF front end is made up of a transmitter and receiver. The transmitter produces a vertically polarized or horizontally polarized transmit pulse at 13.9 GHz. Two transmit power levels can be selected, 10 or 250 watts. The receiver has a vertical and horizontal channel. In each channel, the receive signal is amplified and coherently mixed down to I/Q signals. These signals are passed to the data acquisition module, which performs digital square-law detection. Each sampled signal is then integrated over a .5 second interval and the result is stored to magnetic tape.

The antenna subsection consists of a dual polarized parabolic dish antenna, wave guide, rotary joint, and gimbal. The antenna has a pencil beam with a peak gain of 32 dB and a 2-way equivalent beamwidth of 4° . The gimbal rotates the antenna in azimuth from 0° to 360° and points the antenna in incidence from 0° to 60° . These pointing angles are controlled by the controller subsection with some compensation for the aircraft motion. The controller subsection also sets the radar parameters such as the pulse repetition frequency, transmit pulse length and transmit polarization. Radar specifications are summarized in Table 1.

To monitor any fluctuation in the transmitter and receiver gains during measurements, the transmit pulse is injected into a calibration loop. This loop attenuates the signal to within the dynamic range of the receiver, into which it is directed and sampled. Uncertainties in this measurement combined with uncertainties in the measurements of the altitude, rotary joint losses, waveguide losses, radome losses, attenuators values, and sampling determine the accuracy of the relative calibration. The estimated calibration error has a root mean square error of ± 0.23 dB. The absolute calibration of NUSCAT is performed at JPL by measuring the losses in the antenna subsection components such as the rotary joint and the waveguides, and measuring the absolute gain of the antenna. The antenna gain patterns are determined using a three horn measurement technique at the JPL Antenna Range.

Figure 2 shows the NUSCAT antenna installation on the NASA Ames C-130. During flight the gimbal positions the antenna at a selected incidence angle. Four seconds of data is collected at a given azimuth angle and selected polarization, and then the antenna is rotated 10° in azimuth. This produces a cycloid scan pattern on the ocean surface. The precision of these measurements is determined by the number of independent samples (N) and the signal to noise ratio. Independent samples are generated by the forward motion of the aircraft. However, to increase the number of independent samples or the rate at which they are collected, the transmit frequency is dithered by 100 MHz. For the typical measurement scenario the expected standard deviation due to fading after averaging over independent samples is ± 0.23 dB.

B. C-SCAT

C-SCAT is a vertically polarized C-band pulsed scatterometer developed by the Microwave Remote Sensing Laboratory (MIRSL) at UMASS. This instrument is comprised of four modules: antenna/spinner, transmitter/receiver, digital interface, and computer/data acquisition. Figure 3 shows a general block diagram for this system, and Table I summarizes the specifications.

The antenna/spinner module consists of a microstrip planar array, spinner unit, and shaft encoder. The array is made up of 16 series fed columns, each with 27 elements. A Taylor weighting is applied to the 27 elements resulting in sidelobe levels for the array that are approximately 20 dB down from the main lobe. The main lobe can be frequency steered from 20° to 50° off boresight by changing the transmit frequency from 5.7 GHz to 4.98 GHz, respectively. Over this frequency range the antenna gain varies from 26.4 to 29.1 dB, the E-plane 2-way equivalent beamwidth varies from 4.2° to 6.3° and the H-plane 2-way equivalent beamwidth is 4.5° .

The antenna is laminated to a 48 inch aluminum disk and a hollow shaft is mounted on the other side. This shaft fits up through the bearing housing of the spinner unit. The spinner unit consists of a baseplate on which a dc motor, a 10 bit shaft encoder and the bearing housing are mounted. The motor, shaft encoder and antenna shaft are coupled together with a chain and sprocket assembly. The motor rotates the antenna in azimuth at speeds up to 40 rpm, providing contiguous azimuthal coverage of the surface winds. The shaft encoder monitors the position of the antenna and sends the information to the data acquisition system.

The antenna module is connected to the transmitter/receiver module through a rotary joint and a low loss microwave coaxial cable. The transmitter/receiver module is made up of a temperature controlled transmitter and receiver and a commercial solid state C-band amplifier. The transmitter mixes a 30 MHz IF signal with a local RF oscillator of frequency 4.98 GHz to 5.7 GHz. This signal is pulse modulated, amplified to either 100 mW or 10 W, and routed to the antenna module via the coaxial cable. The pulse duration and the power level of this signal is set by the digital interface module. This module creates the above control signals as well as the pulse repetition frequency, the receive signal, and the

receiver bandwidth selection signal. All these signals are programmable over a 16 bit bus between the digital interface module and the computer.

The two control signals, receiver and receiver bandwidth selection, determine the mode and configuration of the receiver. The receive control signal enables the first stage of the receiver which amplifies, filters, and down-converts the return signal from the antenna module. The down converted signal or IF signal is amplified and passed through one of 5 bandpass filters ranging from 50 KHz to 10 MHz. This filter bank is designed to maintain a minimum signal to noise ratio (SNR) with altitude. The SNR is given by

$$SNR = \frac{P_R}{\kappa T_o \beta F_n} \quad (7)$$

where P_R is the receive power, κ is Boltzman's constant, T_o is the temperature of the receiver, β is the bandwidth of the selected bandpass filter, and F_n is the noise figure of the receiver. Since C-SCAT operates in a beam-filled mode, P_R is inversely proportional to the square of the altitude, H^2 ,

$$P_R \propto \frac{\cos \theta}{H^2}.$$

As the altitude increases the transmit pulse length is increased so that a narrower bandpass filter can be selected to compensate for the decrease in P_R . Figure 4 demonstrates this technique for a NRCS of -25 dB [53]. The receiver bandwidth selection signal selects the filter approximately 3 to 8 times the bandwidth of the transmitted pulse.

Following the filter bank is a 85 dB dynamic range log detector. This detector linearly maps the input IF power (in dBm) to a voltage, which is held by a sample and hold circuit. The output of this circuit is connected to an 12-bit A/D card in the computer/data acquisition module that digitizes this signal. The 12-bit representation of the detected power level is stored to disk along with the 10 bit encoder word. The radar system parameters and the navigation data are also stored to disk. The navigation data provides information about altitude, pitch, yaw, roll, latitude and longitude.

Fluctuations in the gain of the transmitter and receiver are monitored through a calibration loop similar to that of NUSCAT. During a flight the gain typically varies by only .1 dB. The absolute calibration of C- SCAT is performed at UMA SS before and after each aircraft installation. A 1 m trihedral corner reflector is placed in a grassy field and C-SCAT

is mounted on the roof of a building at the beginning of the field. The same RF cables and radome installed on the aircraft are used in the calibration. The range to the corner reflector is measured using a range finder that is accurate to within 2 cm. Calibrations vary less than 1 dB.

Figure 5 shows the C-SCAT antenna installation on the NOAA N42RF P3. The installation on the C-130 is similar and the same radome is used on both aircraft. During a flight, the antenna is mechanically rotated in azimuth to provide contiguous coverage. The incidence angle is varied during flight by changing the frequency of the local oscillator. Both the rotation speed and incidence angle selection are controlled through the computer. The result is that C-SCAT conically scans the ocean surface providing a complete 360° scan approximately every 2 seconds. For each scan, the data is passed through a lookup table that converts the measurement from a log scale to a linear scale and is averaged into seventy-two 5° bins with each bin having approximately 30 samples. The bin size, 5°, was selected since the two-way equivalent beamwidth is approximately 5°.

To reduce the statistical variation of the backscattered power from the ocean surface, several scans are averaged together to produce a stable average of the NRCS. The number of scans averaged represents a trade off between the standard deviation and spatial resolution of the averaged measurement. Since the backscatter power from the ocean surface is exponentially distributed provided that the footprint is large compared to the dominant ocean wave length, the standard deviation is equal to the mean. Incoherently averaging N backscatter measurements reduces the standard deviation by $1/\sqrt{N}$. Depending on the spatial variability of the surface winds or other parameters such as the sea temperature, two or more scans are averaged together.

C. KU-SCAT and C-SCATII

KU-SCAT and C-SCATII are vertically polarized Ku and C-band pulsed scatterometers developed by the MIRSIL at UMASS. These two instruments are similar in design to C-SCAT with these additional capabilities:

- Azimuthal scanning up to 100 rpm,
- Rapid incidence angle scanning,
- Real time data reduction, and

- Single system operation.

Figure 6 shows a general block diagram for these two systems. The two instruments are shown as operating as one system in this diagram, but they can run independently of each other. A summary of the specifications for both radars is given in Table I.

To achieve the increase azimuthal scanning rate, the KU-SCAT and C-SCATII antennas weigh less than the C-SCAT antenna. The KU-SCAT antenna is a frequency scaled version of C-SCAT, thus it is approximately one-third its size and weight. The main lobe of this Ku-band antenna is a pencil beam with a 2-way equivalent beam width of approximately 5° and a gain of approximately 25 dB. It can be frequency scanned in incidence from 20° to 50° by changing the frequency from 14.8 GHz to 12.8 GHz, respectively. Using a similar spinner design as C-SCAT's, the antenna is rotated in azimuth to speeds up to 100 rpm. A 10-bit shaft encoder monitors the position of the antenna and this information is passed to the data acquisition system.

The weight of the C-SCATII antenna was kept down by laminating the same microstrip phase array on a 48 inch aluminum-honeycomb disk rather than an aluminum disk. With this weight reduction, the same C-SCAT spinner design can rotate the new antenna at speeds up to 100 rpm. The performance of this new antenna is the same as the older aluminum-disk version.

Rapid incidence angle scanning was also incorporated into the design of the transmitter/receiver modules for KU-SCAT and C-SCATII. This rapid scanning consists of transmitting and receiving at four times the rate that an independent sample at a fixed incidence angle can be obtained. By changing the incidence by 10° with each pulse, independent samples are collected at 20° , 30° , 40° , and 50° incidence in the time it previously took to obtain only one sample. To accomplish this scanning, the RF local oscillator was replaced with four dielectric resonant oscillators (4 RO's) with frequencies corresponding to 20° , 30° , 40° , or 50° incidence, and a four-port pin diode switch with a switching speed of 150 nsec. With each pulse a different DRO is selected by the switch. As in C-SCAT, the selected DRO is mixed with a IF oscillator at 30 MHz, pulse modulated, amplified and sent to the antenna module. KU-SCAT amplifies the RF signal to either 30 mW or 20 W and C-SCATII amplifies the RF signal to 100 mW or 10 W.

The IF portion of the receiver for both instruments is the same as the C-SCAT receiver IF section. However, part of the RF portion of KU-SCAT was separated from the IF section so that it could be mounted near to the antenna to improve the noise figure of the receiver. This RF front end consists of a transmit/receive switch followed by a low noise amplifier. The box that contains these parts is temperature controlled to prevent severe changes in the gain of the low-noise amplifier with temperature fluctuations. The output is fed back to the receiver through a low loss flexible cable. This signal passes through a RF filter and is down converted to 30 MHz, where it is amplified, passed through a filter bank and detected using a log detector. The C-SCATII receiver is the same as the C-SCAT receiver.

To handle the increased data rate and volume, the data acquisition system is being upgraded. The new system consists of a 382 Hp computer and a VXI card cage containing two 10 MHz 23 bit A/D boards and 2 DSP boards. Each A/D will digitize the video signal from each receiver. The digitized words will be averaged into 5° azimuthal bins and NRCS will be calculated for that bin. The final output of these boards will be the NRCS in 5° azimuthal bins, each consisting of approximately 30 averaged independent samples for each incidence angle. The results will be stored to disk with the corresponding azimuthal position from the shaft encoder and navigation data.

Finally, KU-SCAT and C-SCATII are designed to operate together using this VXI data acquisition system. The two instruments can be mounted in a single rack and together weigh approximately the same as the old C-SCAT system. This will provide a unique opportunity to obtain a comparison data set at Ku- and C-band. Both antennas will simultaneously observe the same sections of the ocean at the four incidence angles. Additionally, KU-SCAT and C-SCATII were also designed to operate separately when both instruments cannot be installed on the same aircraft. In fact, KU-SCAT was installed and flown on the NASA Wallops P3 for initial test flights. The flights verified the system stability and performance. Both systems will be calibrated at UMASS in the spring of 1994.

111. DATA PRESENTATION

Current physically-based and empirical models agree with observations under certain wind regimes and surface conditions; however, none appear to have complete success for all polarizations, incidence angles, and air-sea conditions. For near-surface winds less than $5 \text{ m}\cdot\text{s}^{-1}$ or greater than $20 \text{ m}\cdot\text{s}^{-1}$, the NRCS observations still exhibit a wind dependence but differ in terms of the magnitude and the azimuthal dependence from current models.

In 1991 NUSCAT and C-SCAT collected NRCS data under low-wind conditions during the Surface Wave Dynamics Experiment (SWADE). In 1992 C-SCAT obtained further measurements under low-wind conditions in the Tropical Oceanic Atmospheric Couple Ocean Atmosphere Response Experiment (TOGA COARE) and under high-wind conditions in Hurricane Tina. A presentation of these data follows along with a discussion of the discrepancies between these observations and predicted results from empirical and physically-based models. The objective of these comparisons is not to reject or re-define the model functions shown, but rather to point out differences that are present when considering NRCS measurements collected under conditions that exhibit large spatial variability or steep gradients in the wind field.

A. Low Wind Speed

SWADE, sponsored by the Office of Naval Research (ONR), began in October 1990 and spanned a six month period. Its primary objectives were to improve our understanding of the spatial and temporal evolution of directional wave spectra, wind forcing and wave dissipation, effects of waves on the air-sea coupling mechanisms, and the microwave response of the surface [54]. Figure 7 shows the primary location of the experiment off the coast of Virginia and the locations of the National Oceanographic and Atmospheric Administration's (NOAA) buoys, which provided in-situ measurements such as the wind speed, wind direction, pressure, air temperature, sea temperature, significant wave height and directional or non-directional wave spectra.

With the support of NASA, NUSCAT and C-SCAT were installed on the NASA Ames Research Center's C-130B and flown during the SWADE Third Intensive Observation Period (IOP-3) from 27 February, 1991 to 10 March, 1991. Figure 8 shows the configuration

of NUSCAT and C-SCAT on the C-13011. This aircraft flew ten missions during IOP-3; several observations were collected by the two instruments under low- and moderate-wind conditions.

For moderate-wind conditions, the empirical model CMOD4 agrees well with observations collected with C-SCAT. Figures 9 and 10 plot the upwind and crosswind NRCS measurements at 20°, 30°, 40° and 50° incidence as a function of the 10 m neutral stability wind speed derived from buoy wind measurements, which are colocated within 5 km of the radar observations. The 10 m neutral stability winds are calculated from the measured winds using an algorithm developed by Ezraty [55], which accounts for the effects of air-sea temperature difference on the near-surface stratification. Each NRCS point represents an average of 70 independent samples. With the exception of the 20° upwind data, the mean differences between the predicted CMOD4 results and the C-SCAT observations are less than .5 dB. The larger difference seen with 20° upwind NRCS values, approximately 1.5 dB, could be due to a calibration bias between the two instruments, C-SCAT and the AMI scatterometer. However, the crosswind NRCS measurements at this angle do not show the same bias, but rather fall within a .5 dB mean difference. This indicates that the C-SCAT observations point to a slightly larger upwind/crosswind modulation at 20° incidence than predicted by CMOD4. Though overall, this empirical model function represents the C-SCAT observations for moderate winds fairly well.

Backscatter observations under low-wind conditions, however, are inconsistent with the model predictions. During the mission on 01 March 1991, low- and moderate-wind conditions were encountered. The flight pattern on this day consisted of 12 legs passing over Buoys A and C. Figure 11 summarizes the near-surface conditions at these two locations. The upper panel of Figure 11 shows the 10 meter neutral stability wind speed at Buoy A to be between 3 to 5 $\text{m}\cdot\text{s}^{-1}$ and at Buoy C to be approximately 8 $\text{m}\cdot\text{s}^{-1}$; the lower panel displays the Monin-Obukhov stability parameter, z/L , at Buoy A and C (note: z is evaluated at 10 m). This stability parameter characterizes the stratified conditions and is proportional to the temperature flux and inversely proportional to the cube of the friction velocity. A positive value (downward temperature flux) represents stable conditions and a negative value (upward temperature flux) represents unstable conditions. During the

flight, the stability parameter at Buoy C was approximately 0 (neutrally stable) and at Buoy A varied between 0 and 0.6. The positive z/L values at Buoy A are a consequence of a 3°C air-sea temperature difference. Keller et al. [32] found that such conditions leads to a reduction in the NRCS. However, after further analysis of the same data, Geernaert et al. [35] determined the reduction in the NRCS can be accounted for by comparing the NRCS measurements with the neutral stability winds, which account for the variation in the wind stress drag coefficient with stability. All C-SCAT and NUSCAT measurements will therefore be compared to the 10 m neutral stability winds,

For the conditions *shown* at Buoy C (moderate winds), CMOD4 predicts values close to that of the observations. Figure 12 shows four averaged NRCS scans at 40° incidence obtained with C-SCAT. Each scan consists of approximately 10 consecutive conical scans averaged together so that each 5 degree azimuthal bin is an average of approximately 300 independent samples. The solid line is the predicted NRCS using CMOD4 and the measured 10 m neutral stability wind speed and direction from Buoy C.

For low-wind conditions, though, the observations are inconsistent with model predictions. Figure 13 displays NUSCAT and C-SCAT NRCS measurements collected at 20° incidence and vertical polarization over an entire flight leg from Buoy C to Buoy A [56]. To compare NUSCAT and C-SCAT measurements, the azimuthal scans obtained by C-SCAT during each 3 minute NUSCAT scan period are averaged together and displayed as one scan. The lower panel of this figure plots the azimuthal pointing angle, while the middle and upper panel show the corresponding NRCS measurements collected with C-SCAT and NUSCAT, respectively. The Ku-band measurements each consist of an average of 1000 independent samples and an average signal to noise ratio of 60 dB. The C-band measurements represent an average of 300 independent samples with an average signal to noise ratio of 30 dB.

As the low-wind region is sampled near Buoy A, the Ku-band NRCS decreases dramatically. The SASS-II model function predicts that the difference in the upwind and the crosswind NRCS due to a decrease in wind speed from $8 \text{ m}\cdot\text{s}^{-1}$ to $3 \text{ m}\cdot\text{s}^{-1}$ should be 3.9 dB and 2.6 dB, respectively. However, the Ku-band measurements show a 10 dB drop in the upwind NRCS and a 30 dB drop in the crosswind. Furthermore, the azimuthal

modulation increases to over 25 dB; whereas the SASS-II model predicts that it should decrease with the wind having the value of 2.8 dB at a wind speed of $3 \text{ m}\cdot\text{s}^{-1}$.

The C-band NRCS measurements also decrease from Buoy C to Buoy A. However, the azimuthal modulation does not appear to be as distinct as it is in the Ku-band data. The reduction in this modulation is caused by the large spatial averaging of the C-SCAT data, performed in order to compare the measurements of both radars on a scan by scan basis. For each azimuthal angle, several C-SCAT backscatter samples are averaged over a range in wind speed resulting in smoothing the azimuthal modulation, and since these averages were spatially discrete averages rather than a moving average, discontinuities between the second and third scan resulted. To reduce these effects, only two consecutive conical scans are averaged together. The last two minutes of C-SCAT data shown in Figure 13 are averaged in this manner and presented in Figure 14. The average signal to noise ratio for these measurements is approximately 25 dB. The azimuthal modulation shown in this figure is as large as 22 dB, and the location of the nulls corresponds to the same azimuthal pointing angle as does the location of the Ku-band NRCS nulls in Figure 13. Furthermore, the aircraft only traveled 7.2 km from scan 2 to scan 4, yet there is strong variability in the NRCS scans indicating that the spatial variability of the NRCS at low wind speeds occurs over lengths less than 2 km.

Figure 15 shows more examples of this increased azimuthal modulation at 20° , 30° , 40° , and 50° incidence. The upper two panels, 20° and 30° incidence, display modulations on the order of 20 dB. They also demonstrate a great deal of variability both in magnitude and in position of the nulls from scan to scan, which explains why this modulation was smoothed out in Figure 13 where several of these scans were averaged together. The lower panels, 40° and 50° incidence, also display azimuthal modulations greater than predicted by CMOD4, although they are not quite as large as those in the upper panels. This could be partly due to the low signal to noise ratio in the crosswind direction. Additionally, the missing azimuthal bins, especially in the 50° data, are due to a decrease in the scan rate at high incidence angles. The antenna was spun in azimuth at a speed which would ensure overlapping conical scans, resulting in decrease spin rates at these higher incidence angles. Therefore, when averaging over short time periods as in these plots, the antenna

does not complete a full revolution.

A distinct roll off in the crosswind NRCS can be seen in both the C-band and Ku-band crosswind NRCS as long as C-SCAT's averaging time is kept to within 20 seconds (2 km). To demonstrate model performances in predicting this decrease in the NRCS measurements at Ku- and C-band, the crosswind NRCS measurements obtained with NUSCAT and C-SCAT are compared to the Donelan and Pierson (DP87), SASS-II and CMOD4 model functions. DP87 model was chosen since it predicts an increase in the azimuthal modulation and a rapid decrease in the mean NRCS as low-wind conditions are approached, and also predicts a cutoff wind speed below which the NRCS cannot be measured. For these comparisons only the measurements within 10 km of either Buoy A or C are considered since there is a large wind speed gradient between the two buoys. Furthermore, to prevent smoothing effects, the C-band data is averaged over the shortest distance possible that ensures enough independent samples are collected to obtain a statistically stable NRCS average. Both the data collected by the two radars and the empirical models SASS-II and CMOD4 are normalized to the DP87 model at a 10 m neutrally stable wind speed of $8.1 \text{ m} \cdot \text{s}^{-1}$ to account for any calibration differences between the models and the data. The offsets applied are summarized in Table II. The inputs to the DP87 and SASS-II models are $U(\lambda/2)$ and $U(19.5)$, respectively, where the parameter λ is the Bragg resonant wavelength. These values are calculated from the 10 m neutrally stable wind speed using the wind profile,

$$U(z) = \frac{u_*}{\kappa} \log \frac{z}{z_0}, \quad z_0 \ll z \quad (8)$$

where u_* is the friction velocity, κ is von Karman constant, z is the height of the desired wind measurement, and z_0 is the roughness length necessary to preserve finite shear [57].

Figure 16 compares the Ku-band and C-band crosswind NRCS measurements to DP87, SASS-II and CMOD4 models. In the upper panel, the crosswind Ku-band measurements at 20° , 30° , 40° , and 50° incidence are plotted. The SASS-II model fails to predict the decrease in the crosswind measured values as the wind speed drops below $5 \text{ m} \cdot \text{s}^{-1}$. Qualitatively the DP87 model predicts the same sharp decrease in the crosswind NRCS as seen in the measurements as the wind decreases to 3 to $4 \text{ m} \cdot \text{s}^{-1}$ but appears to underestimate the

actual values. In the lower panel the C-band crosswind NRCS measurements at 20°, 30°, 40°, and 50° incidence are compared to the DP87 and CMOD4 models. The models underestimate the roll off in the measured values with decreasing winds. However, the sharp drop in the data for all four incidence angles and winds between 4 to 3 $\text{m}\cdot\text{s}^{-1}$ is similar to DP87 model predictions for 3 to 2 $\text{m}\cdot\text{s}^{-1}$.

Additional data collected with C-SCAT during TOGA COARE also displays a similar roll off or cutoff as the winds decrease below 3 $\text{m}\cdot\text{s}^{-1}$. This experiment was organized through the TOGA COARE International Project Office at University Center for Atmospheric Research (UCAR) to study the role of the Western Pacific warm water pool in the mean and transient state of the tropical ocean/global atmosphere system. Figure 17 shows the primary location of the experiment and labels the positions of meteorological and oceanic buoys. For this experiment, C-SCAT was installed on the NOAA N42RF P3 and flew twenty-one missions from 01 November 1992 to 22 February 1993. Eight of these missions were concentrated over the Woods Hole Oceanographic Institution (WHOI/US) Improved Meteorological instrumentation (IMET) buoy, which recorded the wind speed, wind direction, air temperature and sea temperature on a 7.5 minute cycle. The sea surface temperature for these flights remained between 29°C and 30°C. The air temperature varied so that the air-sea temperature difference fell between -4° C and 0°C. The more negative temperature differences occurred when the wind was under 2 $\text{m}\cdot\text{s}^{-1}$ resulting in Z/L values as negative as -8. Such unstable conditions increase the surface layer turbulence, and have the effect of roughening the sea surface which could result in higher NRCS values. But as the data will show, a roll off in the NRCS is still evident as the wind decreases below 3 $\text{m}\cdot\text{s}^{-1}$.

Figures 18 and 19 present C-SCAT upwind and crosswind data collected at 20°, 30°, 40°, and 50° incidence during the TOGA COARE and SWADE flights. These data were spatially filtered, keeping only those measurements within 10 km of a buoy. Each point shown is an average of two conical scans (approximately 70 independent samples per 5-degree azimuthal bin). These data were plotted as a function of the colocated 10 m neutral stability wind. The solid lines in these figures represent the predicted NRCS values using CMOD4. For winds less than 6 $\text{m}\cdot\text{s}^{-1}$, the measured upwind NRCS departs from the

CMOD4 values. The data display a large increase in the variability and a rapid roll off as the wind decreases. The scatter in the data at these low-wind speeds exceeds that which can be explained by fading statistics and measurement errors in the wind speed. Similarly, the crosswind NRCS data exhibit these characteristics with even more scatter at the low-wind speeds. This variability indicates that the surface winds and their interaction with the ocean surface, temporally and spatially vary at low-wind speeds. Characterizing this variation and including its effects in a model is needed to better describe the NRCS.

To further exemplify the variation and roll off of the NRCS at low winds, Figure 20 plots the measured upwind/crosswind NRCS ratio and the predicted values of the CMOD4 and DP87 models. A sea surface temperature of 29.5°C is used for the DP87 model since much of the low-wind speed data were collected during TOGA COARE. The upper two panels of this figure display 20° and 30° data while the lower two panels show 40° and 50° data. The signal to noise ratio for the 40° and 50° degree measurements was very low as the winds decreased below 6 m·s⁻¹, and therefore large upwind/crosswind NRCS values are not expected. However, the 20° and 30° incidence measurements display large azimuthal modulations as low-wind speeds are approached. This demonstrates that the crosswind NRCS rolls off much quicker than the upwind NRCS. Additionally, the data once again show scatter as large as 15 dB. Neither model seems to correctly predict these results, but the DP87 unlike the CMOD4 model predicts increasing upwind/crosswind NRCS values for the low-wind speeds.

B. High Wind Speed

In September 1992 the NOAA Hurricane Research Center (HRC) sponsored a series of flights through Hurricane Tins, which was centered off the west coast of Mexico at approximately 12°N and 107°W. The NOAA P3 aircrafts, N42RF and N43RF, flew several missions through the eye of this hurricane. With support from NASA and NOAA, CSCAT was installed on N42RF and participated in these missions. The UMSS Stepped Frequency Microwave Radiometer, SFMR, was also installed on N42RF and provided estimates of the rain rate and wind speed [58][59].

Figure 21 summarizes the wind and rain conditions of one of the penetrations of the eyewall on 21 September 1992. The upper panel plots the measured flight level wind

speed (solid line) and the SFMR estimated 10 m neutral stability wind speed. The middle panel displays the SFMR estimated rain rate. The lower panel shows the radial distance from the center of the hurricane. For this pass, the aircraft flew at 5000 feet entering the northern side of the hurricane and punched right through the eye to exit on the southern side. The recorded flight level winds exceeded 60 knots with a 1 knot low within the eye. Most of the precipitation occurred on the southern wall with rain rates as high as $20 \text{ mm} \cdot \text{hr}^{-1}$. C-SCAT collected data at 50° incidence for the entire leg. Due to the sharp spatial gradients in the wind speed, no more than 4 scans were averaged together in order to prevent smoothing effects as seen in the SWADLE data (Figure 13) from occurring.

Figure 22 shows a time series image of these averaged NRCS measurements and the associated flight level winds. The x-axis of the image is C-SCAT's azimuthal pointing angle relative to magnetic North; the y-axis is the navigation time that corresponds to the NRCS and flight level wind measurements. For each averaged scan, azimuthal bins ranging from 0° to 359° relative to North are displayed; that is, each averaged conical scan is stretched out on the x-axis and stack in time on the y-axis. The center of the image (180°) is the approximate heading of the aircraft. The flight level wind direction measurements are shown by the black trace overlaid on the image. The NRCS values have been adjusted to account for the 2-way attenuation the transmitted signal suffers due to precipitation.

The northern and southern edges of the eyewall arc distinctly marked. The mean NRCS drops from -11 dB to -20 dB at the northern edge (17:25) and increases from -20 dB to -9 dB at the southern edge (19:30). Similarly, the corresponding flight level winds go from 60 knots down to 1 knots back up to 60 knots. SFMR estimates the maximum 10 m neutral stability wind on the northern side to be $25 \text{ m} \cdot \text{s}^{-1}$ (17:24) and on the southern side to be $33 \text{ m} \cdot \text{s}^{-1}$ (17:31). Besides marking the eyewalls, the azimuthal modulation in the image provides a clear picture of the wind direction since the maximum value marks the upwind direction. As the eyewall is approached the upwind direction slowly shifts from 80° to 70° , and then rapidly shifts to 270° as the southern eyewall is reached.

This type of image provides useful real-time information during a flight to determine the extent of the storm, provide information about shears in the vertical wind profile when

combined with flight level data, and clearly define the region of the eye. Closer detail of the magnitude, azimuthal modulation, and spatial variability however can be better seen in Figures 23 and 24 which plot each individual averaged NRCS scan for the above flight leg. Each point represents an average of approximately 200 independent samples. The SFMR 10 m neutral stability wind estimate and the time period over which the scan is averaged is given at the top of each plot. Two noticeable features are seen in these figures: the mean NRCS increases with the 10 m neutral stability wind while the azimuthal modulation decreases, and smoothing effects due to spatial averaging over sharp wind gradients are evident. To better characterize the decreasing azimuthal modulation, Figures 25 and 26 plot the upwind and crosswind NRCS measurements, respectively, as a function of the 10 m neutral stability wind speed. The measurements shown are from flights legs on 21 September and 22 September not including those observations made in the presence of precipitation. Additionally, the solid lines represent the CMOD4 NRCS predictions. The 20° and 30° upwind NRCS measurements shown in the upper panels of Figure 25 agree the best with CMOD4. However, the slope of the upwind NRCS observations for all four angles with increasing wind speed is less than predicted especially at the higher incidence angles. At $25 \text{ m}\cdot\text{s}^{-1}$ CMOD4 overestimates the upwind NRCS at 50° by more than 5 dB. The crosswind NRCS measurements in Figure 26 also display less sensitivity with wind speed and lower values than the CMOD4 predictions, but are closer to CMOD4 than the upwind NRCS measurements. The net effect is it appears that the upwind NRCS is reaching a saturation level, especially at the higher incidence angles, but more NRCS data at wind speeds greater than $30 \text{ m}\cdot\text{s}^{-1}$ are needed to determine the validity of a saturation wind speed.

IV. FUTURE DIRECTION OF SCATTEROMETRY

As has been demonstrated, the off-nadir microwave backscatter from the ocean surface displays a strong dependence with the near surface wind vector. Figures 27 and 28 summarize the C-SCAT upwind and crosswind NRCS measurements collected over wind speeds ranging from 1 to $30 \text{ m}\cdot\text{s}^{-1}$; the corresponding CMOD4 model predictions is overlaid on these plots. For the moderate wind cases shown, the CMOD4 empirical model agrees with C-SCAT observations with the exception of a 1.5 dB bias between the 20° upwind

NRCS measurements and CMOD4. However, inconsistencies exist between the model predictions and the observations for low- and high-wind conditions.

It is these discrepancies that define what some of the future roles of airborne scatterometers should be. At low winds, the measurements display strong spatial variability in terms of the azimuthal modulation with significant changes often occurring over distances less than a kilometer. Airborne scatterometers such as C-SCAT and NUSCAT are capable of obtaining NRCS measurements with spatial resolutions on this order, and thereby can accurately sample this variability. A better understanding of these effects and their relationship with the wind speed, wind direction, and perhaps other parameter such as surface temperature, atmospheric stability, wind stress, wave age, and long waves will aid in the development of more rigorous physically-based models.

In particular the low-wind speed data presented gives qualitative support to Donelan and Pierson's suggestion that viscosity of the water is an important parameter at low-wind speeds. Viscosity prevents the growth of capillary-gravity waves and creates a cutoff wind speed for scatterometry that depends on the sea surface temperature [47]. The sharp rollofs in NRCS measurements collected with C-SCAT and NUSCAT appear to support this concept. Additionally, C-SCAT data collected in SWADE show a higher cutoff than that collected in TOGA COARE. The sea surface temperature in SWADE was between 6° to 19°C while in TOGA COARE it was between 29° to 30° C. The lower cutoff in warmer waters agrees with DP87 predictions in terms of the effects of temperature. Of course, other parameters such as stability and the air-sea temperature must be isolated before concrete conclusions can be drawn.

On the other end of the wind spectrum, airborne scatterometers can play a significant role in monitoring severe storms such as hurricanes. The wind fields in these systems often have steep spatial gradients that will not permit satellite-based systems to accurately map the wind field without smoothing out the results. Airborne scatterometers, however, are capable of high enough resolution to accomplish these tasks. The high wind data obtained with C-SCAT during Hurricane Tina demonstrate the ability of such a radar system to acquire the necessary measurements. These NRCS observations show increasing values as the wind increases above 25 m-s* indicating that wind estimates could be derived. There

was some evidence of the sensitivity decreasing and a saturation beginning to occur, but more data above $30 \text{ m}\cdot\text{s}^{-1}$ is needed to validate these conclusions. Nevertheless, the measurements clearly outlined the surface structure giving a real time estimation of the intensity and extent of the hurricane. Additionally the azimuthal modulation was quite distinct permitting accurate determination of the wind direction.

Overall, the backscatter measurements with these airborne systems show a strong dependence on the wind. Future collection and analysis of high resolution airborne scatterometer data under low- and high-wind conditions will help to resolve the issues presented, and the knowledge gained can be incorporated into existing model functions, allowing for accurate wind estimation using scatterometry. One example of an airborne system suited for this research is the combined Ku-/C-band system KUSCAT/CSCATII presented. This system incorporates high conical scan rates up to 100 rpm, rapid incidence angle sweeping up to 30 kHz, and multiple frequencies centered around the AMI and NSCAT satellite scatterometers to link or distinguish features of the NRCS at C- and Ku-band.

ACKNOWLEDGEMENTS

The authors wish to acknowledge Bob Weller and the National Science Foundation for supplying the IMET buoy data and Andrew Paylor for his assistance with the C-SCAT measurements during TOGA COARE.

This work was supported by the National Aeronautics Space Agency grant NAG W-1112.

REFERENCES

- [1] R. K. Moore, "Radar determination of winds at sca", *Proceedings of the IEEE*, vol. 67, no. 11, 1979.
- [2] M. I. Skolnik, *Radar Handbook*, chapter 12, pp. 18-28, McGraw-Hill, New York, 1990.
- [3] M. I. Skolnik, *Radar Handbook*, chapter 11, pp. 2-3, McGraw-Hill, New York, 1990.
- [4] M. I. Skolnik, *Radar Handbook*, chapter 12, pp. 20-22, McGraw-Hill, New York, 1990.
- [5] F. 'I'. Ulaby, R. K. Moore, and A. K. Fung, *Microwave Remote Sensing Active and Passive*, vol. 2, pp. 757-779, Artech House, Norwood, MA, 1986.
- [6] W. J. Plant and G. L. Geernaert, *Surface Waves and Fluxes*, vol. 2, chapter 12, pp. 195-213, Kluwer Academic Publishers, 1990.
- [7] D. E. Kerr, *Propagation of Short Radio Waves*, Dover Publications, [95].
- [8] C. R. Grant and B. S. Yaplee, "Backscattering from water and land at centimeter and millimeter wave lengths", *Proceedings of the Institute of Radio Engineers*, vol. 45, pp. 976-982, 1957.
- [9] W. S. Ament, F. C. MacDonald, and R. D. Shewbridge, "Radar terrain reflections for several polarizations and frequencies, in 1959 Symposium on Radar Return, University of New Mexico, Albuquerque, 1959.
- [10] J. C. Daley, "Wind dependence of radar sea return", *Journal of Geophysical Research*, vol. 78, pp. 7828-7833, 1973.
- [11] G. R. Valenzuela, M. B. Laing, and J. C. Daley, "Ocean spectra for the high-frequency waves from airborne radar measurements", *Journal of Marine Research*, vol. 29, pp. 69-84, 1971.
- [12] G. A. Bradley, *Remote sensing of ocean winds using a radar scatterometer*, PhD thesis, University of Kansas, 1971.
- [13] J. P. Claassen, R. K. Moore, H. S. Fung, and W. J. Pierson, "Radar sea return and the radscat satellite anemometer", in *Proc. OCEANS '72, IEEE Int. Conf. Rec.*, Engineering in the Ocean Environment (IEEE Publication 72 CHO660-1OCC), Newport, RI, Sept. 1972.
- [14] R. K. Moore and W. J. Pierson, "Worldwide oceanic wind and wave predictions using a satellite radar radiometer", *Journal of Hydronautics*, vol. 5, pp. 52-60, 1971.
- [15] J. D. Young, "Active microwave measurement from space of sea-surface winds", *IEEE Journal of Oceanic Engineering*, vol. OE-2, no. 4, 1977.
- [16] W. J. Pierson, W. E. Marlatt, Z. H. Burns, and W. R. Johnson, "Oceans and atmosphere in Skylab deep investigations summary", NASA Scientific and Technical Information NASA SP-390, NASA, 1978.
- [17] L. C. Schroeder, "Radscat calibration data report", NASA Calibration Report NASA TM X-73900, NASA, 1976.
- [18] W. L. Jones, L. C. Schroeder, and J. L. Mitchell, "Aircraft measurements of the microwave scattering signature of the ocean", *IEEE Transactions on Antennas and Propagation*, vol. 25, no. 1, 1977.
- [19] W. L. Jones and L. C. Schroeder, "Radar backscatter from the ocean: Dependence upon surface friction velocity", *Boundary Layer Meteorology*, vol. 13, pp. 133, 1977.
- [20] L. C. Schroeder, P. R. Schaffner, J. L. Mitchell, and W. L. Jones, "Aircraft radscat 13.9 GHz measurements and analysis: Wind-speed signature of the ocean", *IEEE Journal of Oceanic Engineering*, vol. 10, no. 4, 1985.
- [21] W. L. Grantham, E. M. Bracalente, W. L. Jones, and J. W. Johnson, "The Seasat-a satellite scatterometer", *IEEE Journal of Oceanic Engineering*, vol. 2, no. 2, 1977.
- [22] W. L. Jones, L. C. Schroeder, D. H. Boggs, E. M. Bracalente, R. A. Drown, G. J. Dome, W. J. Pierson, and F. J. Wentz, "The Seasat-a satellite scatterometer: The geophysical evaluation of remotely sensed wind vectors over the ocean", *Journal of Geophysical Research*, vol. 87, no. C5, 1982.

- [23] "Special issue", *Journal of Geophysical Research*, vol. 87, no. C3, April 1982.
- [24] J. D. Hawkins and P. G. Black, "Seasat scatterometer detection of gale-force winds near tropical cyclones", *Journal of Geophysical Research*, vol. 88, no. C3, pp. 9723-9730, 1990.
- [25] W.T. Liu and W. G. Large, "Determination of surface stress by seasat-sass: A case study with jasin data", *Journal of Physical oceanography*, vol. 11, no. 12, pp. 1603-1611, 1981.
- [26] J. Davison and D. E. Harrison, "Comparison of seasat scatterometer winds with tropical pacific observations", *Journal of Geophysical Research*, vol. 95, no. C3, pp. 3403-3410, 1990.
- [27] F. Feindt, V. Wismann, W. Alpers, and W. C. Keller, "Airborne measurements of the ocean radar cross section at 5.3 ghs as a function of wind speed", *Radio Science*, vol. 21, pp. 845-856, 1986.
- [28] H. Masuko, M. Okamoto, M. Shimada, and S. Niwa, "Measurement of microwave backscattering signatures of the ocean surface using x-band and ka-band airborne scatterometers", *Journal of Geophysical Research*, vol. 91, no. C11, pp. 13065-13083, 1986.
- [29] F. Li, W. Large, W. Shaw, E. J. Walsh, and K. Davidson, "Ocean radar backscatter relationship with near-surface winds: A case study during fasinex", *Journal of Physical Oceanography*, vol. 19, pp. 342-353, 1989.
- [30] M. C. Colton, *The Dependence of Radar Backscatter on the Energetics of the Air-Sea Interface*, Phi thesis, Naval Postgraduate School, Monterey, CA, 1989.
- [31] W. C. Keller, W. J. Plant, and D. E. Weissman, "The dependence of x band microwave sea return on atmospheric stability and sea state", *Journal of Geophysical Research*, vol. 90, no. C1, pp. 1019-1029, 1985.
- [32] W. C. Keller, V. Wismann, and W. Alpers, "Tower-based measurements of the ocean c band radar backscattering cross section", *Journal of Geophysical Research*, vol. 94, no. C1, pp. 924-930, 1989.
- [33] D. E. Weissman, W. J. Plant, K. L. Davidson, and R. A. Brown, "Relating the microwave radar cross section to the sea surface stress: Developing a new model function", in *OCEANS 91 Proceedings*, Honolulu, HI, October 1991.
- [34] D. E. Weissman, "Dependence of the microwave radar cross section on ocean surface variables: Comparison of measurements and theory using data from the frontal air-sea interaction experiment", *Journal of Geophysical Research*, vol. 95, no. C3, pp. 3387-3398, 1990.
- [35] G. L. Geernaert and W. C. Keller, "On the wind power law and atmospheric stability effects in ocean scatterometry", *ISPRS Journal of Photogrammetry and Remote Sensing*, vol. 47, pp. 369-386, 1992.
- [36] M.R. Keller, W. C. Keller, and W. J. Plant, "A wave tank study of the dependence of x band cross sections on wind speed and water temperature.", *Journal of Geophysical Research*, vol. 97, no. C4, pp. 5771-5792, 1992.
- [37] "Special section: The saxon-fpn experiment", *Journal of Geophysical Research*, vol. 99, no. C5, 1994.
- [38] European Space Agency, "Cmod4 model description", Electrosiences Report ER-TN-EA-GP-1 120, European Space Agency, 1993.
- [39] P. Woiceshyn, T. Yu, and W. Gemmill, "Use of ers-1 scatterometer data to derive ocean surface winds at nmc", in *American Met. Soc. 13th Conf. on Weather Analysis and Forecasting Including Symposium on Flash Floods*, Vienna, Virginia, August 1993.
- [40] F.M. Naderi, M. H. Frelich, and D. G. Long, "Spaceborne radar measurements of wind velocity over the ocean -- an overview of the nscat scatterometer system", *Proceedings of the IEEE*, vol. 79, no. 6, pp. 850-866, 1991.
- [41] W. J. Plant and G. L. Geernaert, *Surface Waves and Fluxes*, vol. 2, chapter 11, Kluwer Academic Publishers, 1990.

- [42] J. W. Wright, 'A new model for sea clutter', *IEEE Transactions on Antennas and Propagation*, vol. 16, pp. 217-223, 1968.
- [43] F. G. Bass, L. M. Fuks, A. I. Kalmykov, I. P. Ostrovsky, and A. D. Rosenberg, 'Very high frequency radiowave scattering by a disturbed sea surface part 1: Scattering from a slightly disturbed boundary', *IEEE Transactions on Antennas and Propagation*, vol. 16, pp. 554, 1968.
- [44] S. O. Rice, 'Reflections of electromagnetic waves from slightly rough surfaces', *Comm. Pure Appl. Math*, vol. 4, pp. 351, 1951.
- [45] C. Cox and W. Munk, 'Statistic of the sea surface derived from sun glitter', *Journal of Marine Research*, vol. 13, no. 2, pp. 198-227, 1954,
- [46] G. R. Valenzuela, 'Theories for the interaction of electromagnetic and oceanic waves - a review', *Boundary Layer Meteorology*, vol. 13, pp. 61-85, 1978.
- [47] M. A. Donelan and W. J. Pierson, 'Radar scattering and equilibrium ranges in wind-generated waves with application to scatterometry', *Journal of Geophysical Research*, vol. 92, no. C5, pp. 4971-5029, 1987.
- [48] W. J. Plant, "A two-scale model of short wind-generated waves and scatterometry", *Journal of Geophysical Research*, vol. 91, no. C9, pp. 10735-10749, 1986.
- [49] S. L. Durden and J. F. Vesecky, "A physical radar cross section model for a wind driven sea with swell", *IEEE Journal of Oceanic Engineering*, vol. OE-10, pp. 445-451, 1985.
- [50] A. K. Fung and G. W. Pan, 'A scattering model for perfectly conducting random surfaces: I. model development', internal *Journal of Remote Sensing*, vol. 8, no. 11, pp. 1579-1605, 1987.
- [51] K. S. Chen and D. E. Weissman, 'A backscattering model for ocean surface', *IEEE Transactions on Geoscience and Remote Sensing*, vol. 30, no. 4, pp. 811-817, 1992.
- [52] F. J. Wentz, S. Peteherych, and L. A. Thomas, 'A model function for ocean radar cross section at 14.6 GHz', *Journal of Geophysical Research*, vol. 89, no. C3, pp. 3689, 1984.
- [53] D. J. McLaughlin, *Remote Sensing of the Ocean Surface with C- and Ku-Band Airborne Scatterometers*, PhD thesis, University of Massachusetts, 1989.
- [54] R. A. Weller, M. A. Donelan, M. G. Briscoe, and N. E. Huang, "Riding the crest: A tale of two wave experiments", *Bulletin American Meteorological Society*, vol. 72, pp. 163-183, 1991.
- [55] R. Ezraty, "Etude de l'algorithme d'estimation de la vitesse de frottement a la surface de la mer", ESA Contract 85.2.42.5000, IFREMER, June 1993.
- [56] S. C. Carson, *Airborne Measurements of Radar Backscatter from the Ocean Surface at C-Band*, PhD thesis, University of Massachusetts, 1993.
- [57] W. J. Plant and G. L. Geernaert, *Surface Waves and Fluxes*, vol. 1, p. 106, Kluwer Academic Publishers, 1990.
- [58] Peter G. Black and Calvin L. Swift, "Airborne stepped frequency microwave radiometer measurements of rainfall rate and surface wind speed in hurricanes", in *22nd Conference On Radar Meteorology*, Zurich, Switzerland, Sept 1984.
- [69] K. M. St. Germain, *Applications of Spectral Microwave Radiometry to Sensing of Sea Ice and the Ocean Surface*, PhD thesis, University of Massachusetts, 1993.

FIGURE CAPTIONS

Figure 1. NUSCAT SYSTEM DIAGRAM

Figure 2. NUSCAT antenna installation on the NASA Ames C-130.

Figure 3. CSCAT SYSTEM DIAGRAM

Figure 4. C-SCAT signal to noise ratio versus aircraft altitude. The bandwidths shown are in MHz.

Figure 5. CSCAT antenna installation on the NOAA N42RF P3.

Figure 6. KUSCAT/CSCAT SYSTEM DIAGRAM

Figure 7. Location of SWADE experiment site. The position of the NOAA buoys A, C, E, and N are shown.

Figure 8. C-SCAT and NUSCAT configuration on the NASA AMES Research Center's C-130B.

Figure 9. C-SCAT upwind NRCS measurements obtained during SWADE under moderate-wind conditions. The measurements shown are colocated within 5 km of one of the NOAA buoys. The buoy measured wind speeds are converted to 10 m neutral stability winds. The CMOD4 model function is shown as a solid line.

Figure 10. C-SCAT crosswind NRCS measurements obtained during SWADE under moderate-wind conditions. The measurements shown are colocated within 5 km of one of the NOAA buoys. The buoy measured wind speeds are converted to 10 m neutral stability winds. The CMOD4 model function is shown as a solid line.

Figure 11. The upper and middle panel displays the buoy measured neutral stability wind speed (referenced to 10 m height) and direction and the lower panel plots the Monin-Obukhov stability parameter for March 01 flight during SWADE. Times and dates shown are GMT.

Figure 12. C-SCAT 40° data collected near Buoy C on March 01 flight. The solid line represents the CMOD4 model function. The wind speed was approximately $7 \text{ m}\cdot\text{s}^{-1}$ at 180° from North.

Figure 13. Simultaneous C-SCAT and NUSCAT data collected at 20° vertical polarization during the March 1 flight line from Buoy A to Buoy C during SWADE. Each C-SCAT scan shown above is approximately a 3 minute average of several consecutive conical scans.

Figure 14. C-SCAT data collected near Buoy A on March 01 flight. The wind speed was approximately $4 \text{ m}\cdot\text{s}^{-1}$.

Figure 15. C-SCAT NRCS measurements at 20°, 30°, 40°, and 50° incidence are shown. The 10 m neutral stability winds were less than $5 \text{ m}\cdot\text{s}^{-1}$.

Figure 16. Ku- and C-band crosswind NRCS measurements obtained by NUSCAT and C-SCAT at 20°, 30°, 40°, and 50° and vertical polarization during SWADE over low- and moderate-wind conditions compared with estimated values from the Donelan and Pierson model (DP-87) and SASS-11, and CMOD4.

Figure 17. Location of the primary experiment area in TOGA COARE.

Figure 18. CSCAT upwind NRCS measurements from TOGA COARE and SWADE are plotted to demonstrate the variability and rolloff of the NRCS as low-wind speeds are approached. Each point consists of approximately 70 independent samples and is colocated within 10 km of a buoy. The measured buoy winds are converted to 10 m neutral stability winds.

Figure 19. CSCAT crosswind NRCS measurements from TOGA COARE and SWADE are plotted to demonstrate the variability and rolloff of the NRCS as low-wind speeds are approached. Each point consists of approximately 70 independent samples and is colocated within 10 km of a buoy. The measured buoy winds are converted to 10 m neutral stability winds.

Figure 20. CSCAT upwind/crosswind NRCS ratio from TOGA COARE and SWADE are plotted to demonstrate the variability and rolloff of the NRCS as low-wind speeds are approached. Each point consists of approximately 70 independent samples and is colocated within 10 km of a buoy. The measured buoy winds are converted to 10 m neutral stability winds.

Figure 21. The measured flight level wind speed, estimated rain rate from SFMR and the radial distance to the center of the hurricane are shown for the flight leg through Hurricane Tina on 21 September 1991 at 17:02:00 GMT.

Figure 22. C-SCAT NRCS image of a penetration through Hurricane Tina on 21 September 1991 at 17:02:00 GMT. The flight level wind speed measurements are shown in the left panel. The image is a time series of NRCS scans stretched out in azimuth on the x-axis and stacked in time on the y-axis. The flight level wind direction is the black line overlaid on top of the image.

Figure 22. C-SCAT NRCS measurements for the penetration run shown in the image. Each plot is a time sequence of NRCS scans. The upper right panel shows the beginning of the leg. Following through to the lower right panel which is just prior to breaking through the northern eyewall. The SFMR 10 m neutral stability wind estimates and the time period for each scan is labeled at the top of the plots.

Figure 23. C-SCAT NRCS measurements for the penetration run shown in the image. Each plot is a time sequence of NRCS scans. The upper right panel is just shows the penetration of the northern eyewall. Following through to the lower right panel where the southern eyewall is penetrated. The SFMR 10 m neutral stability wind estimates and the time period for each scan is labeled at the top of the plots.

Figure 24. C-SCAT upwind NRCS measurements at 20°, 30°, 40°, and 50° incidence for hurricane flights on 21 September 1992 and 22 September 1992. The 10 m neutral stability wind was estimated using SFMR. Each NRCS point represents an average of approximately 70 independent samples. The measurements were filtered to exclude any observations made in the presence of precipitation.

Figure 25. C-SCAT crosswind NRCS measurements at 20°, 30°, 40°, and 50° incidence for hurricane flights on 21 September 1992 and 22 September 1992. The 10 m neutral stability wind was estimated using SFMR. Each NRCS point represents an average of approximately 70 independent samples. The measurements were filtered to exclude any observations made in the presence of precipitation.

Figure 26. C-SCAT upwind NRCS measurements at 20°, 30°, 40° and 50° versus the corresponding 10 m neutral stability wind speed. The solid line is the predicted upwind NRCS value using CMOD4.

Figure 27. C-SCAT crosswind NRCS measurements at 20°, 30°, 40° and 50° versus the corresponding 10 m neutral stability wind speed. The solid line is the predicted upwind NRCS value using CMOD4.

TABLE CAPTIONS

Table 1. Radar Specifications

Table 2. Offsets applied to CMOD4, SASSII, C-SCAT data, and NUSCAT data to normalize these values to the DP87 model at $8.1 \text{ m}\cdot\text{s}^{-1}$. The values are in dB.

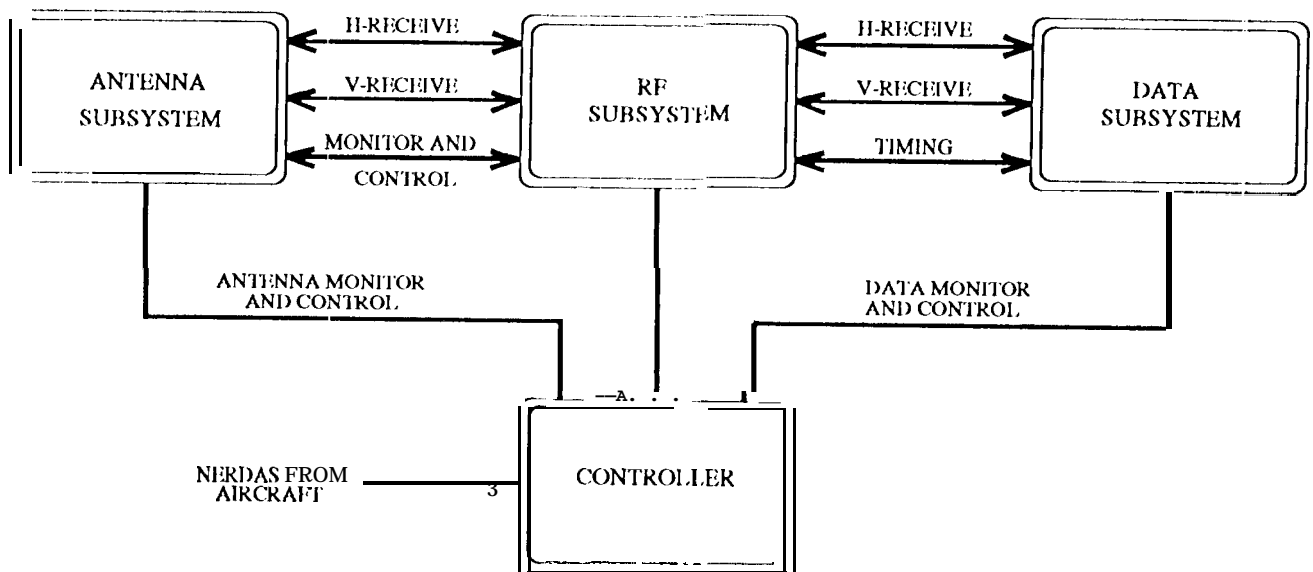


Fig. 1.

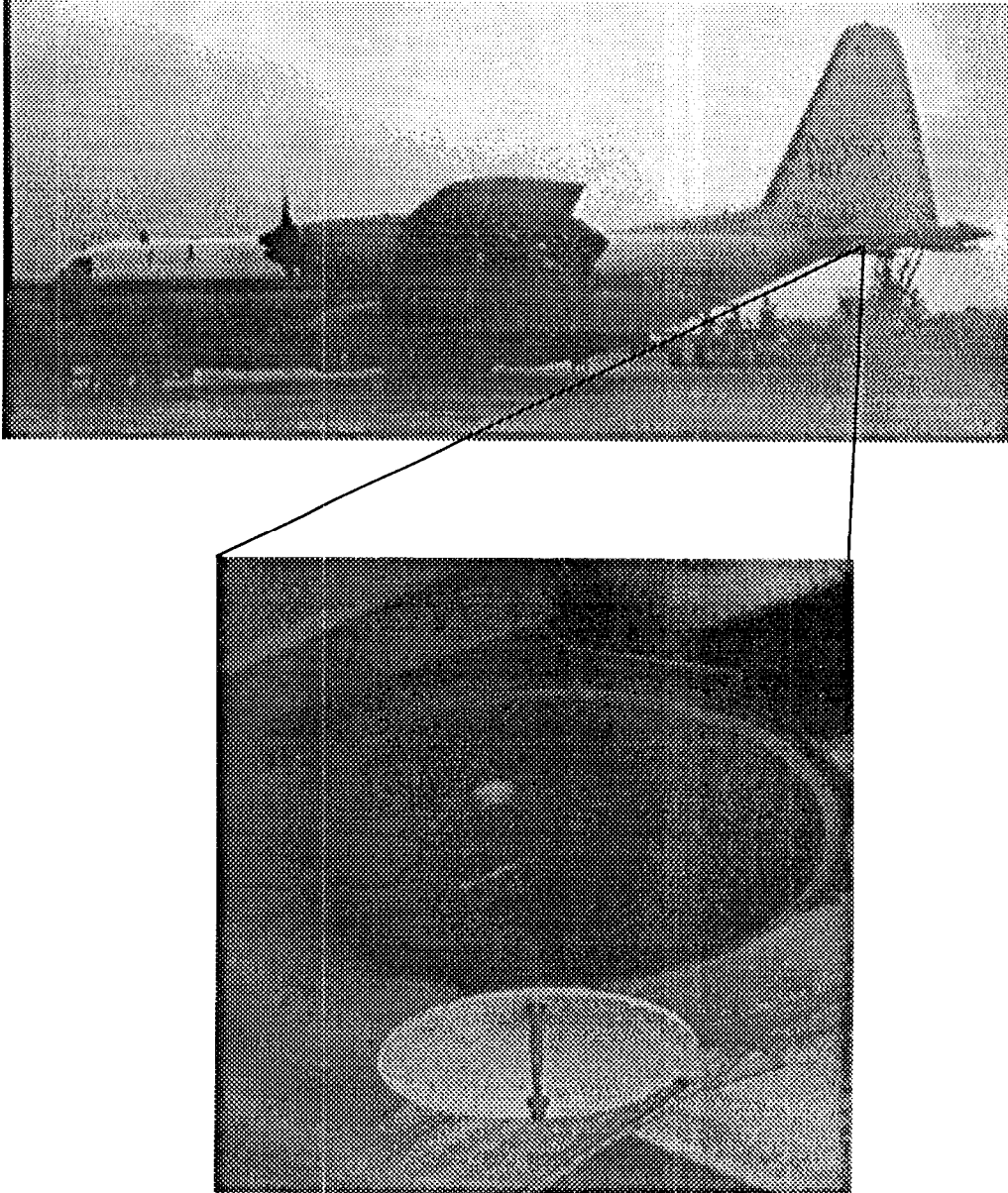


Fig. 2.

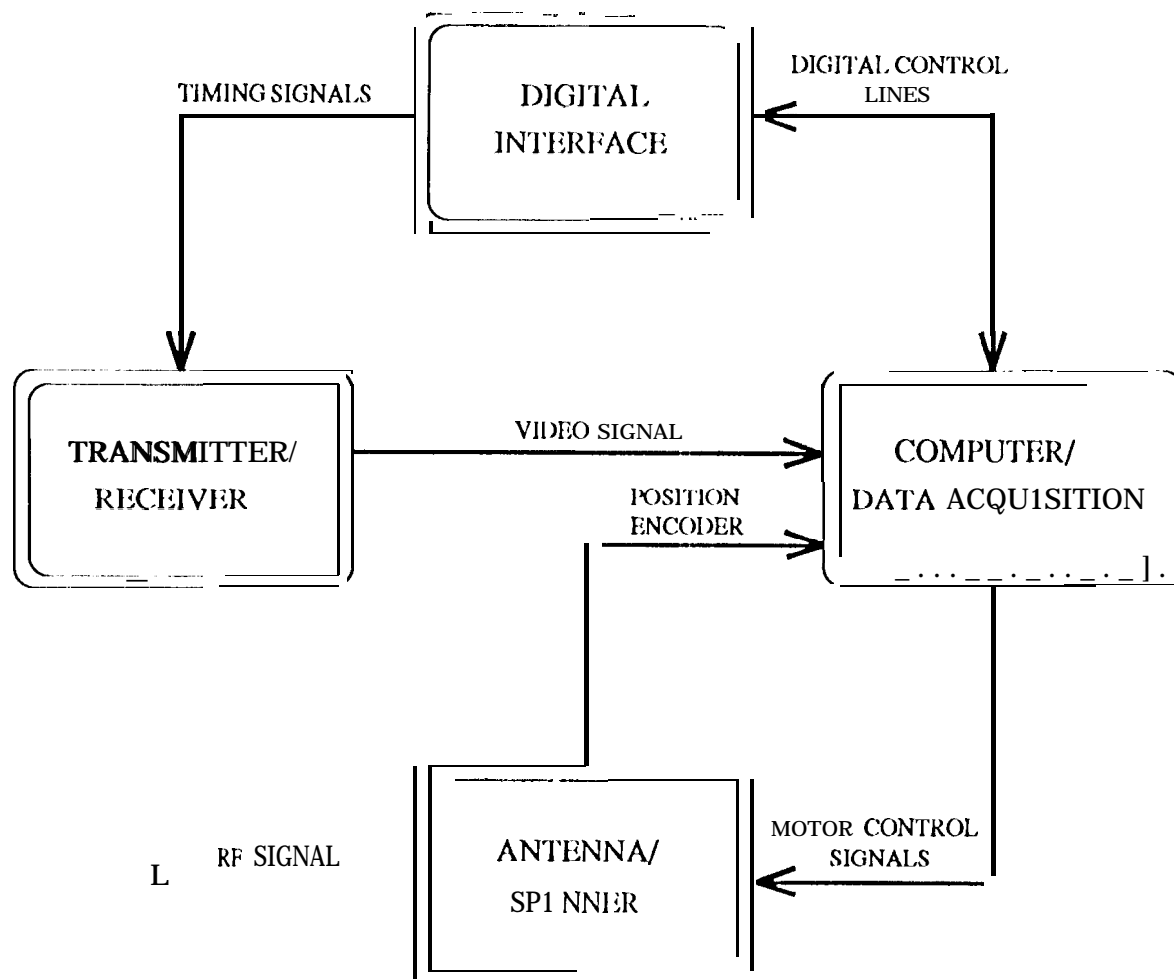


Fig. 3.

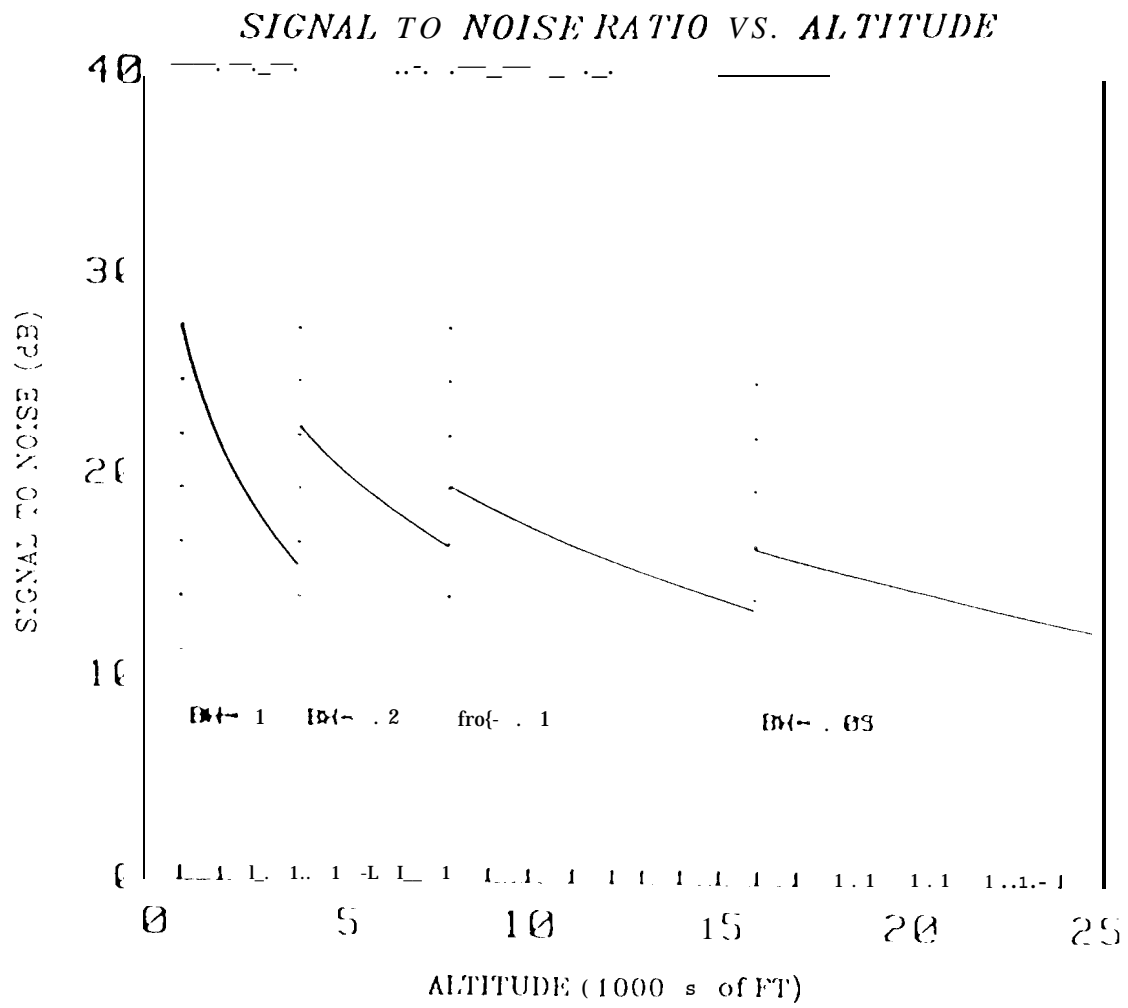


Fig. 4.

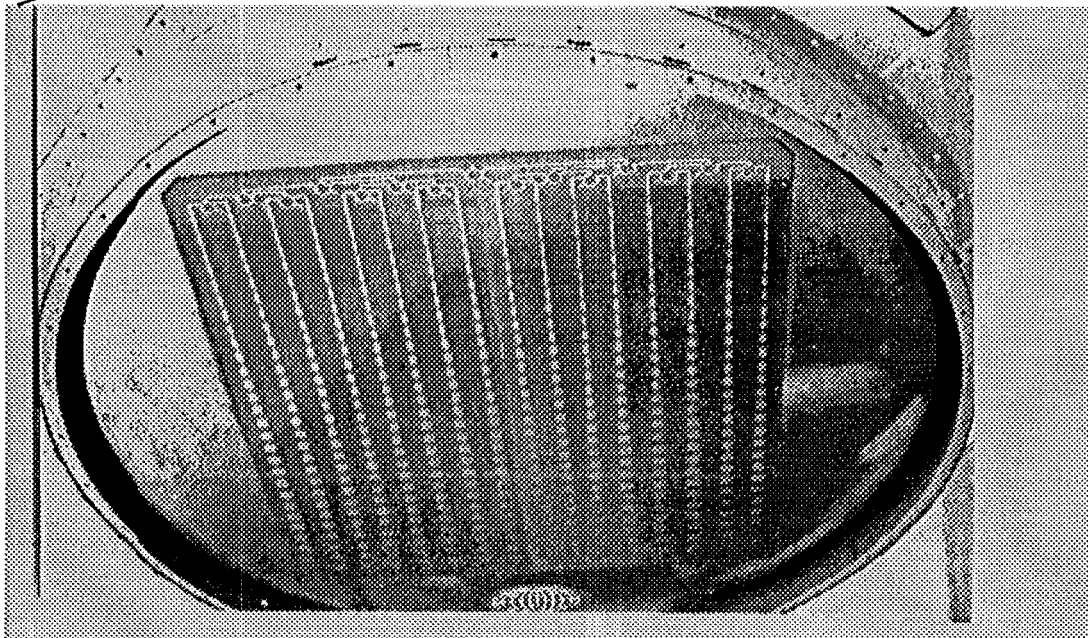


Fig. 5.

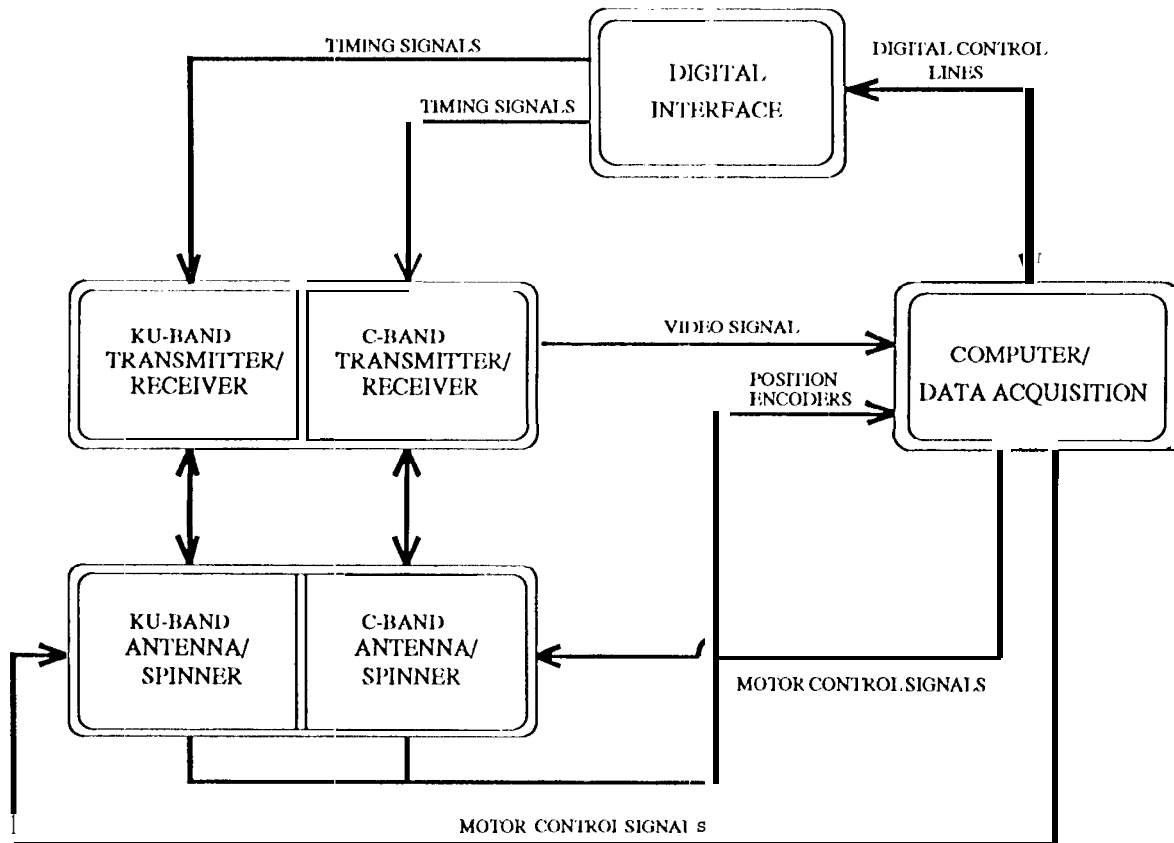


Fig. 6.

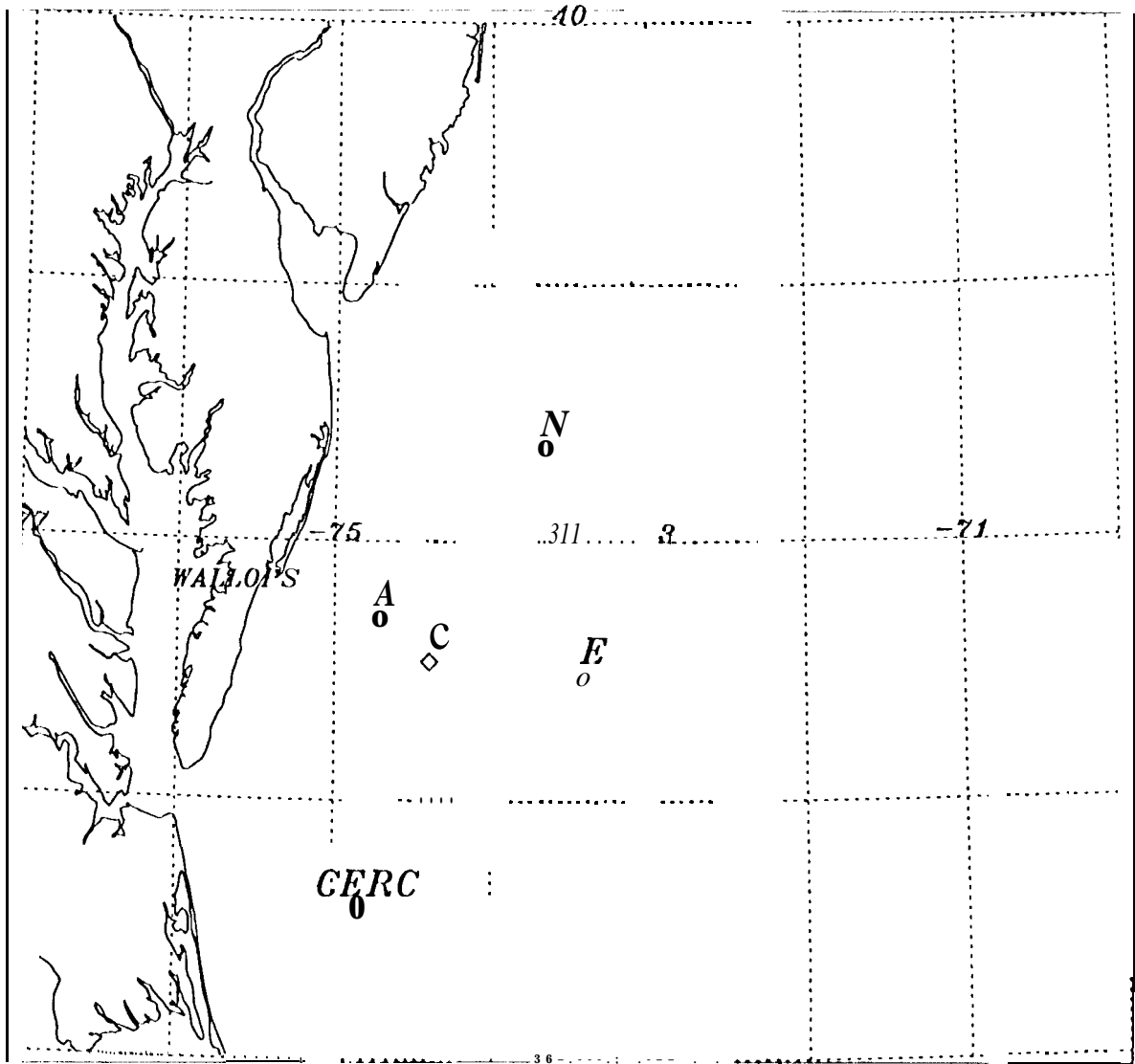


Fig. 7.

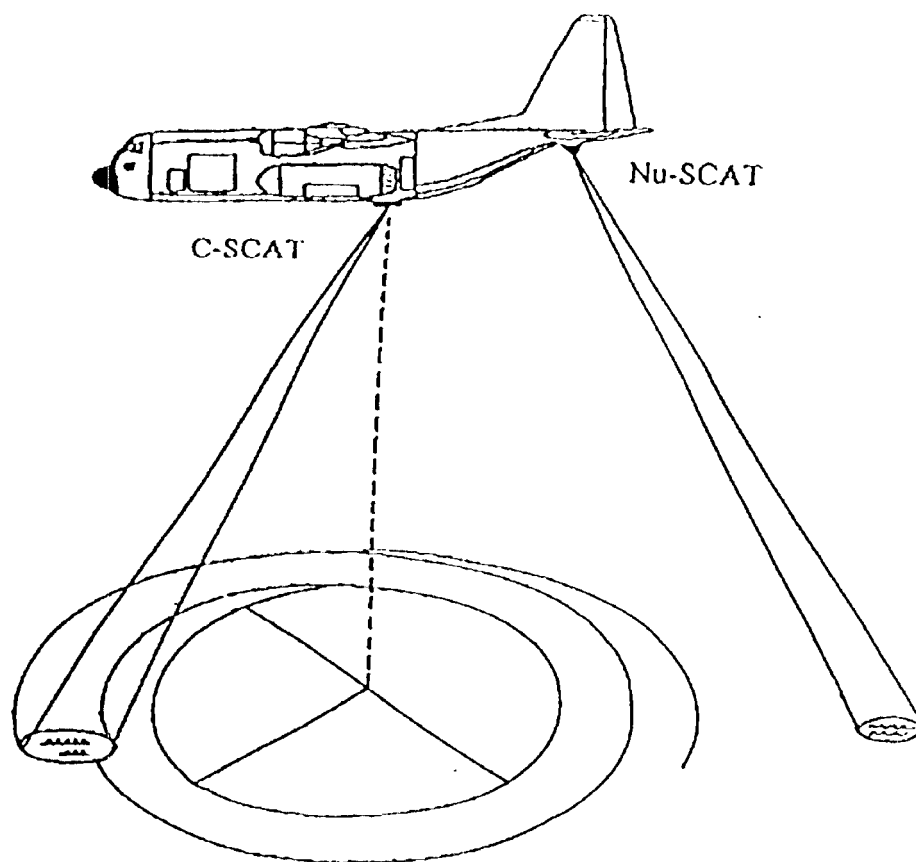


Fig. 8.

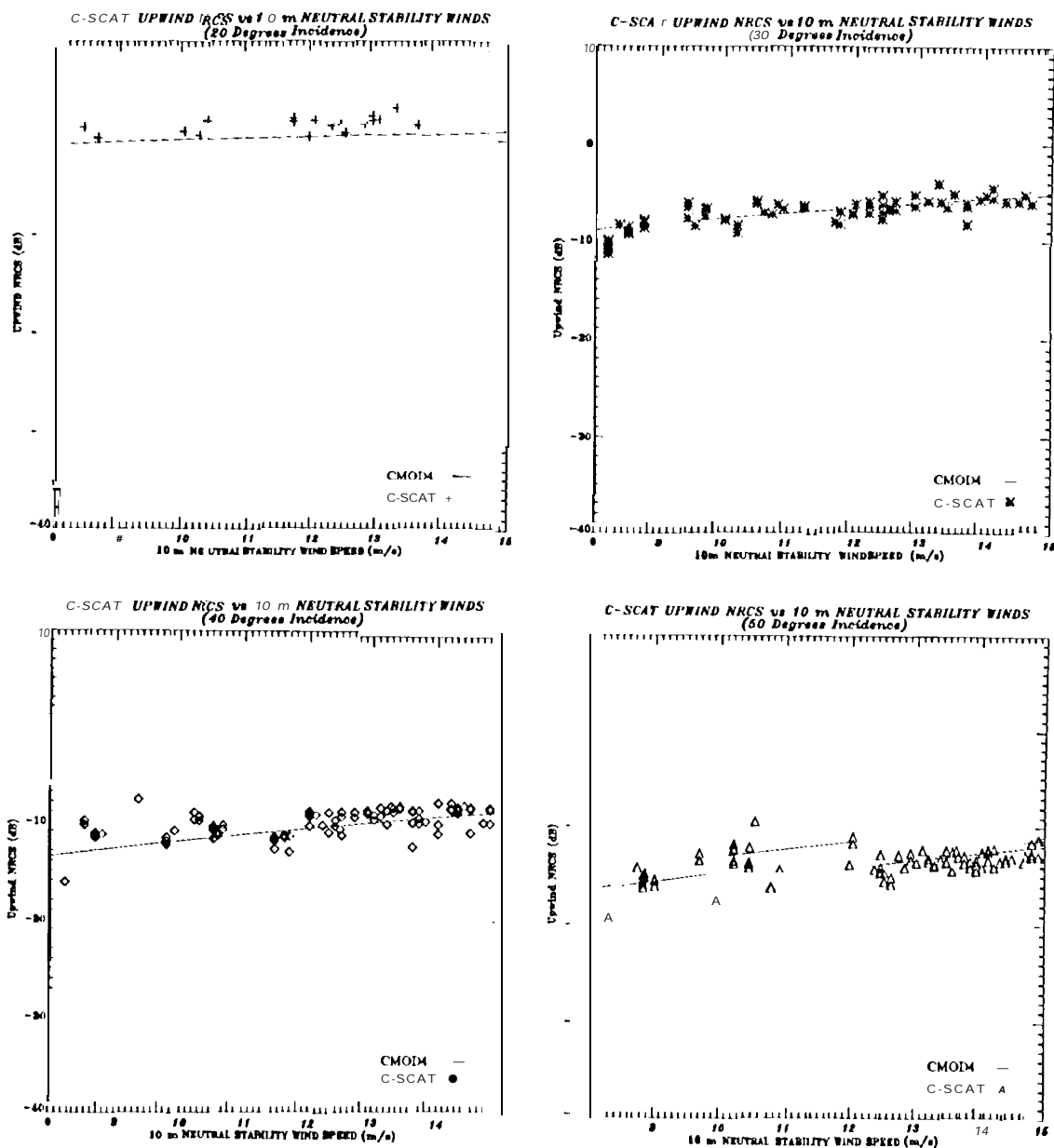


Fig. 9.

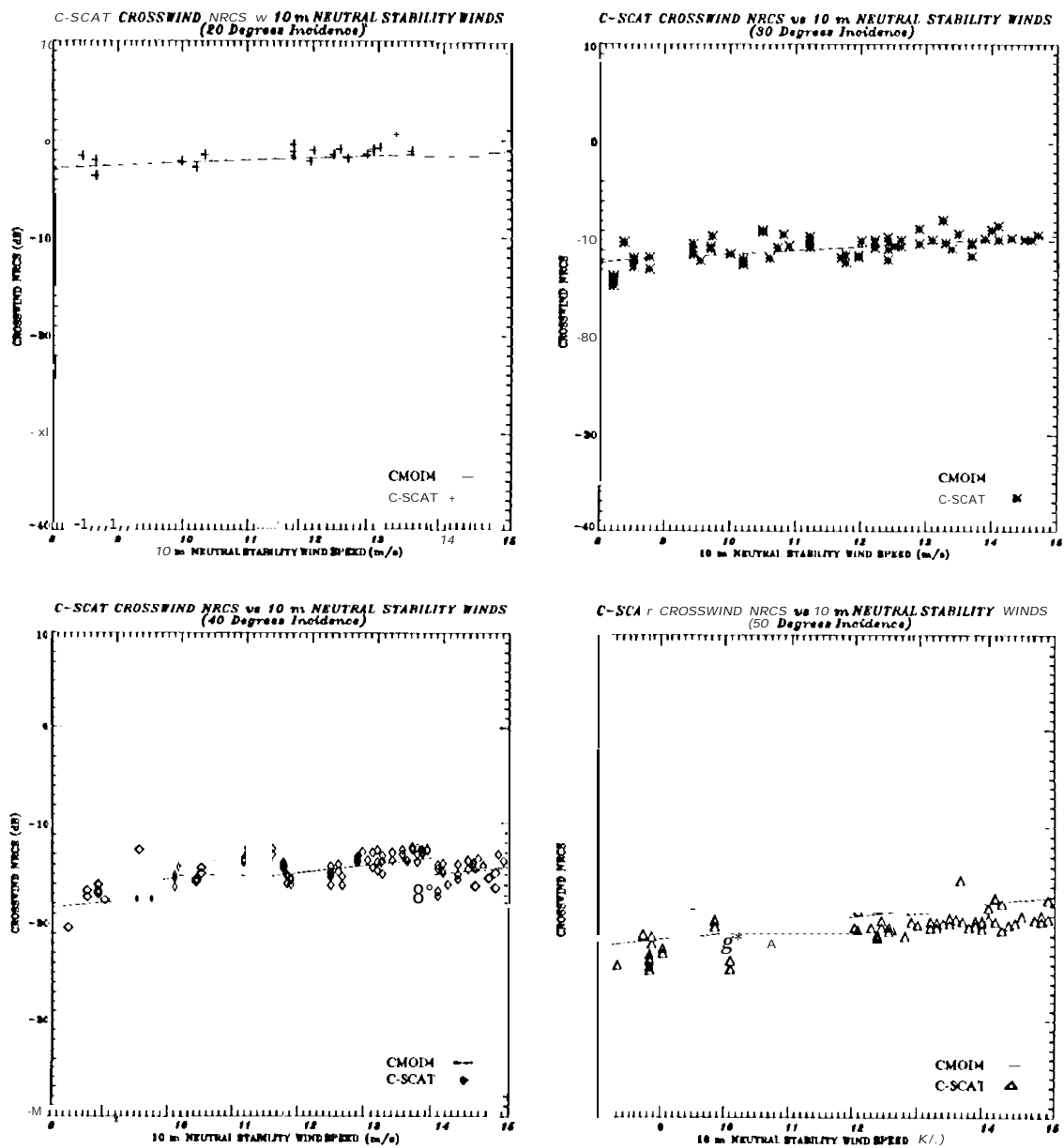


Fig. 10.

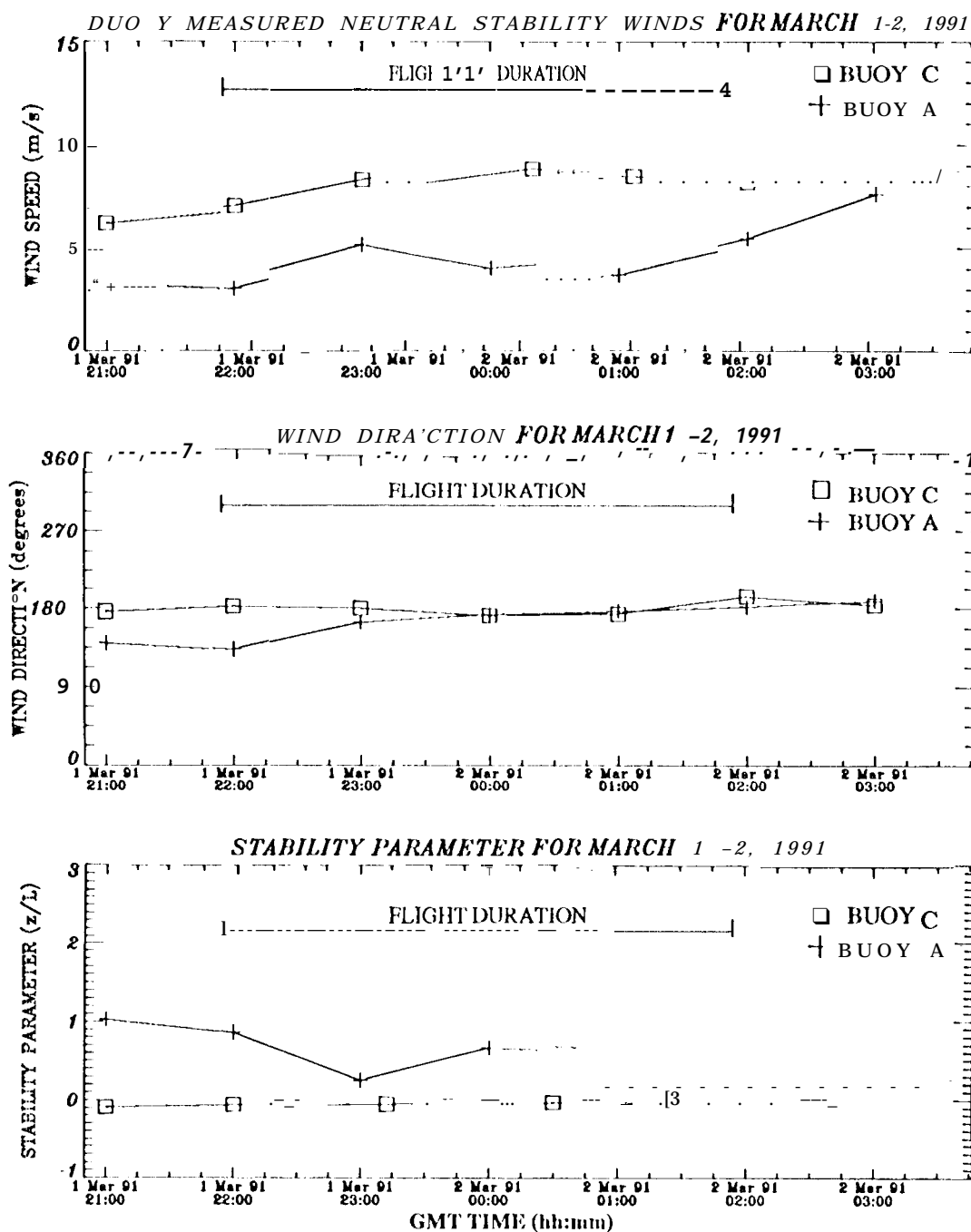


Fig. 11

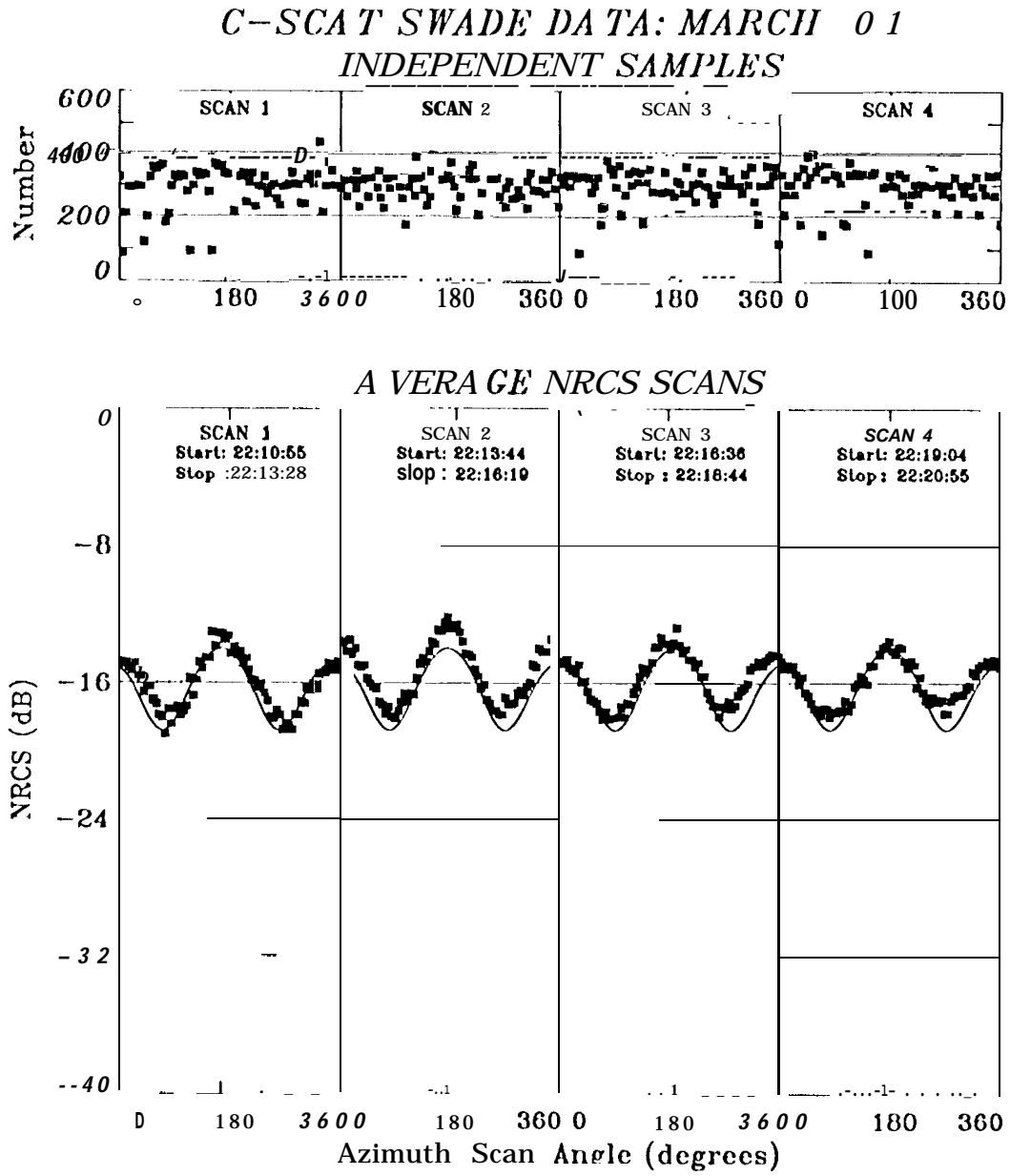


Fig. 12.

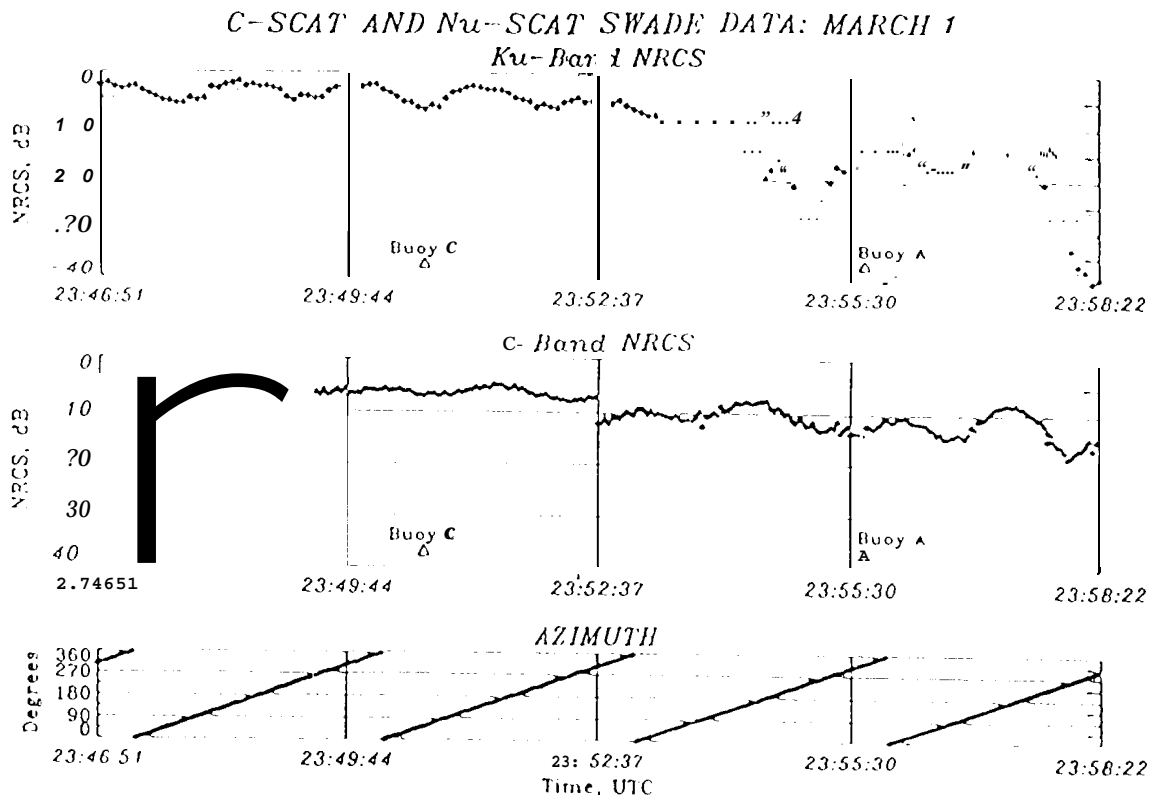


Fig. 13.

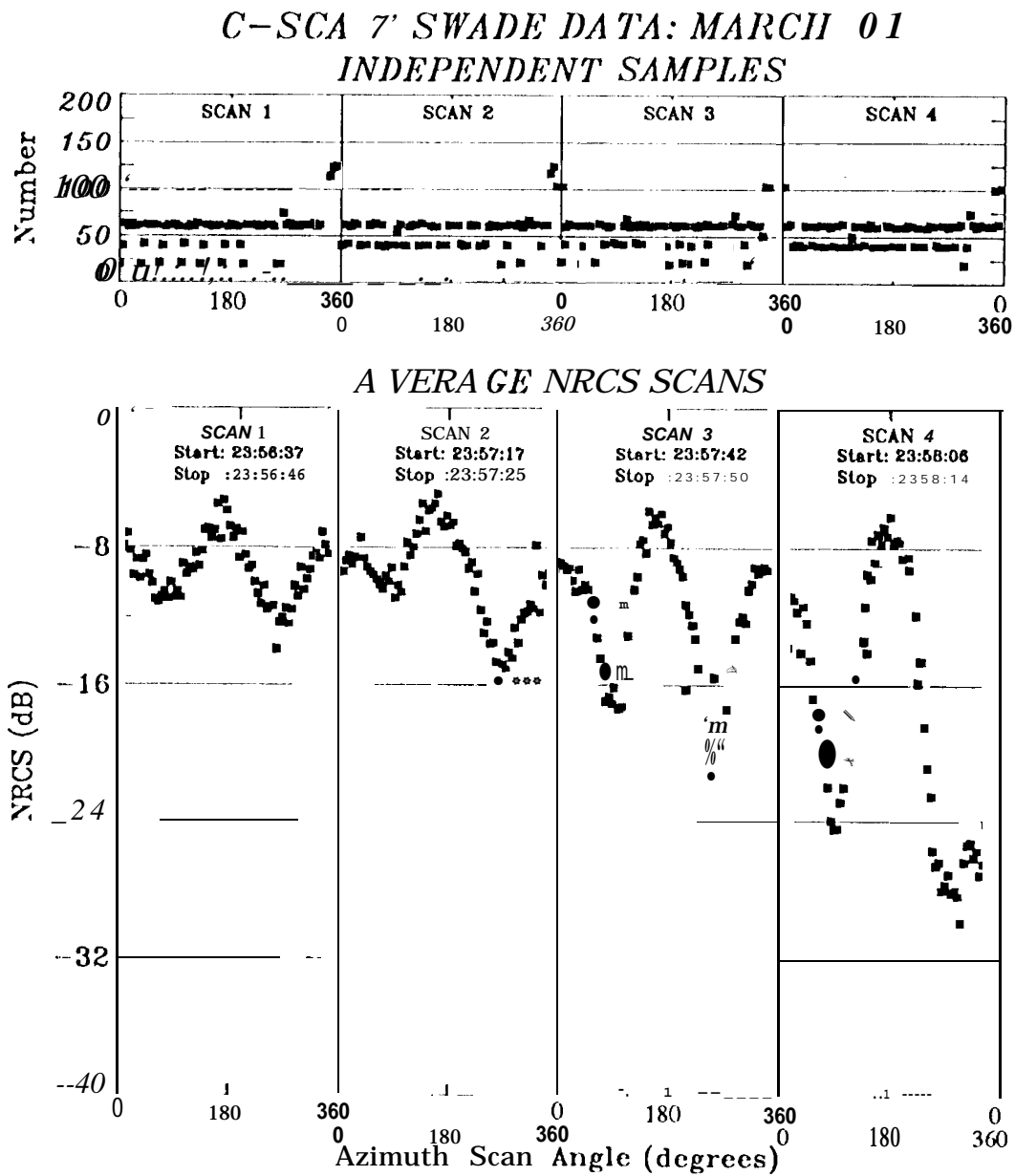


Fig. 14.

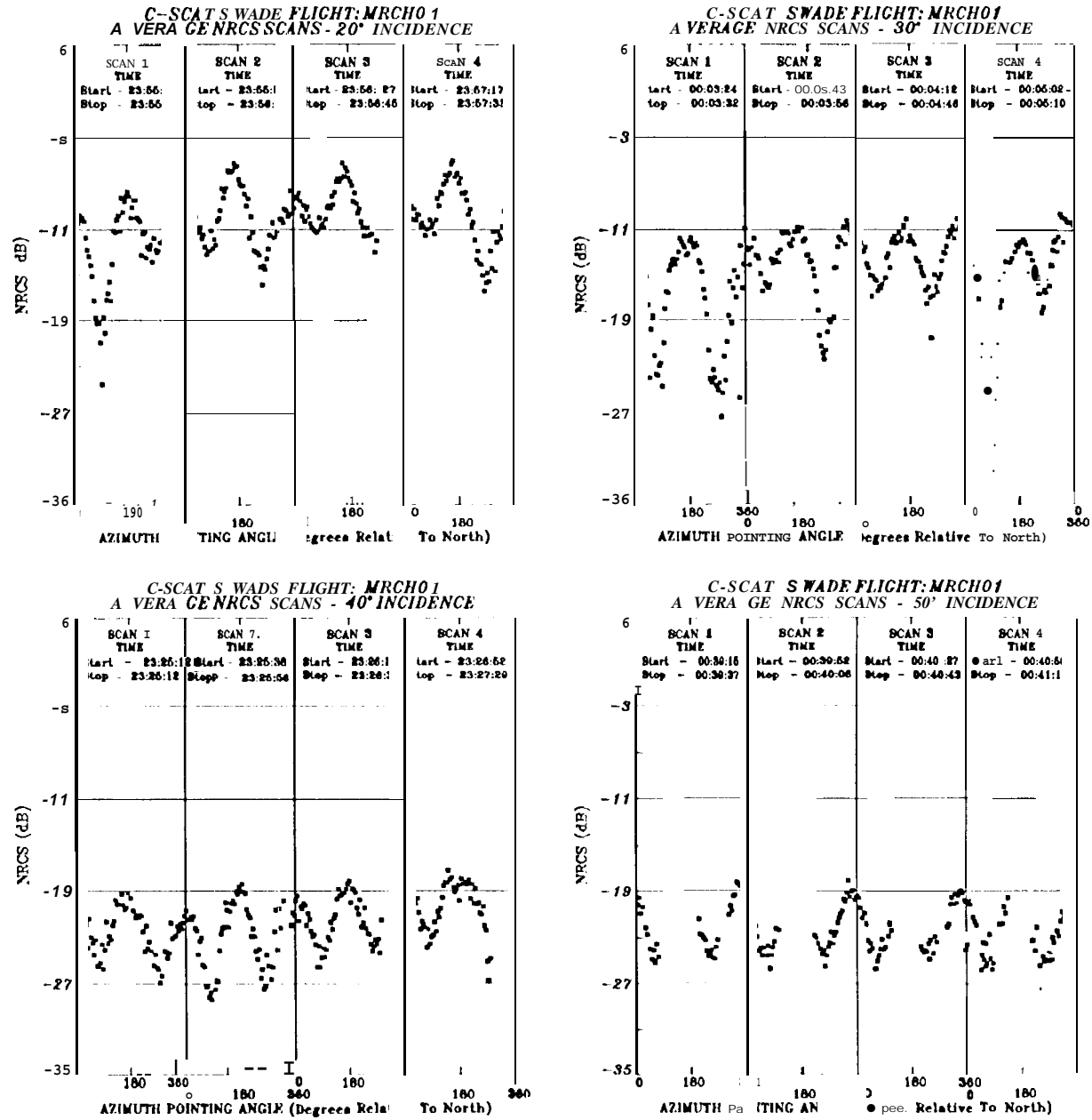


Fig. 15.

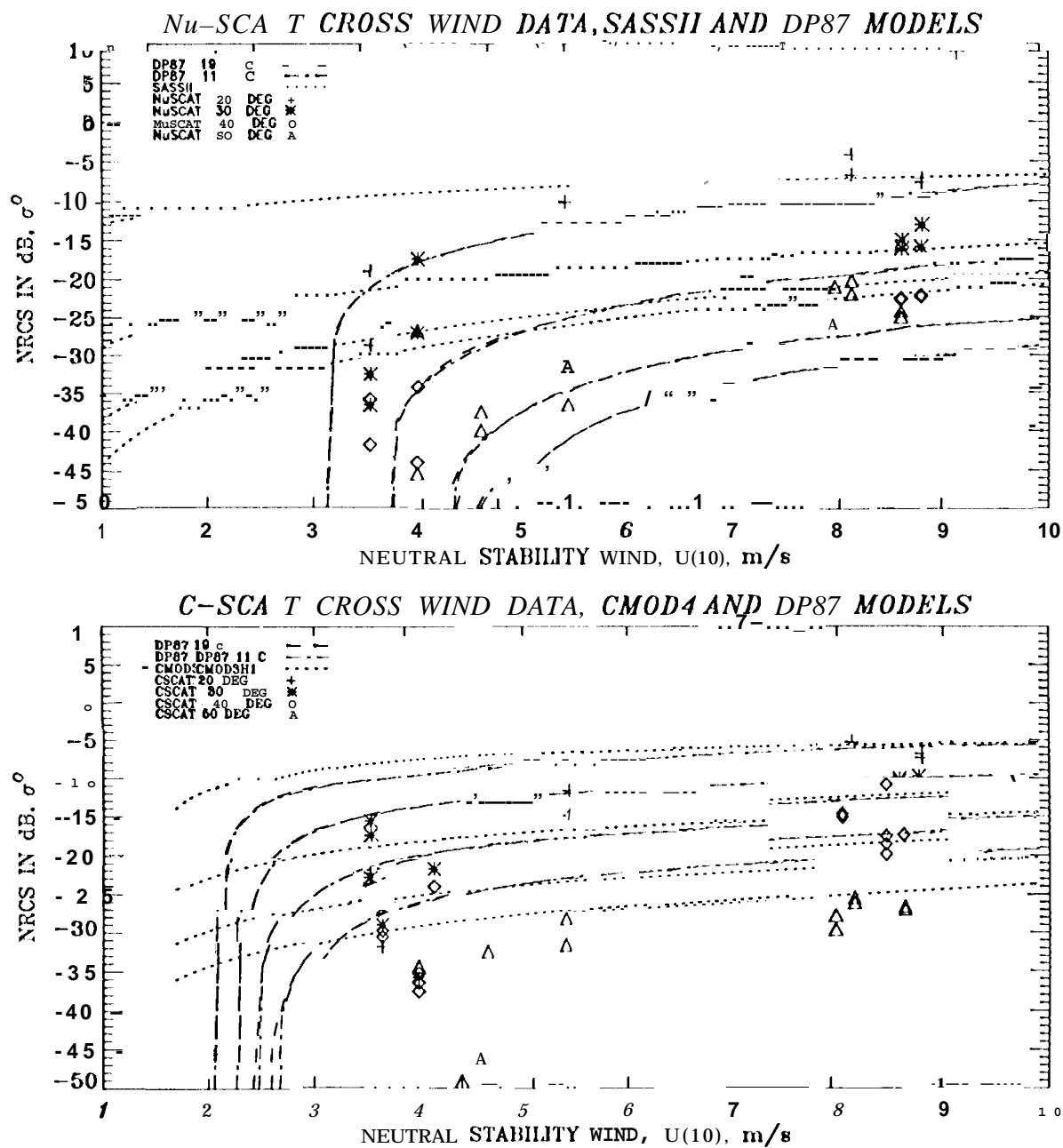


Fig. 16.

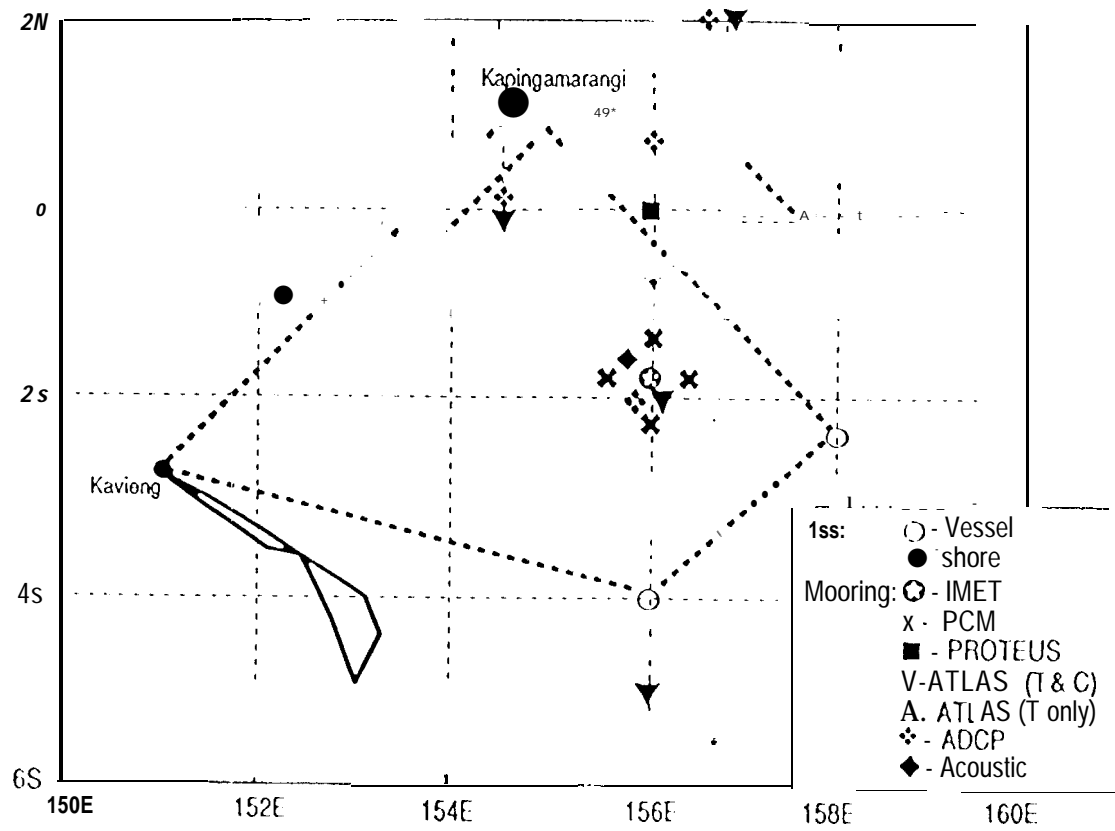


Fig. 17.

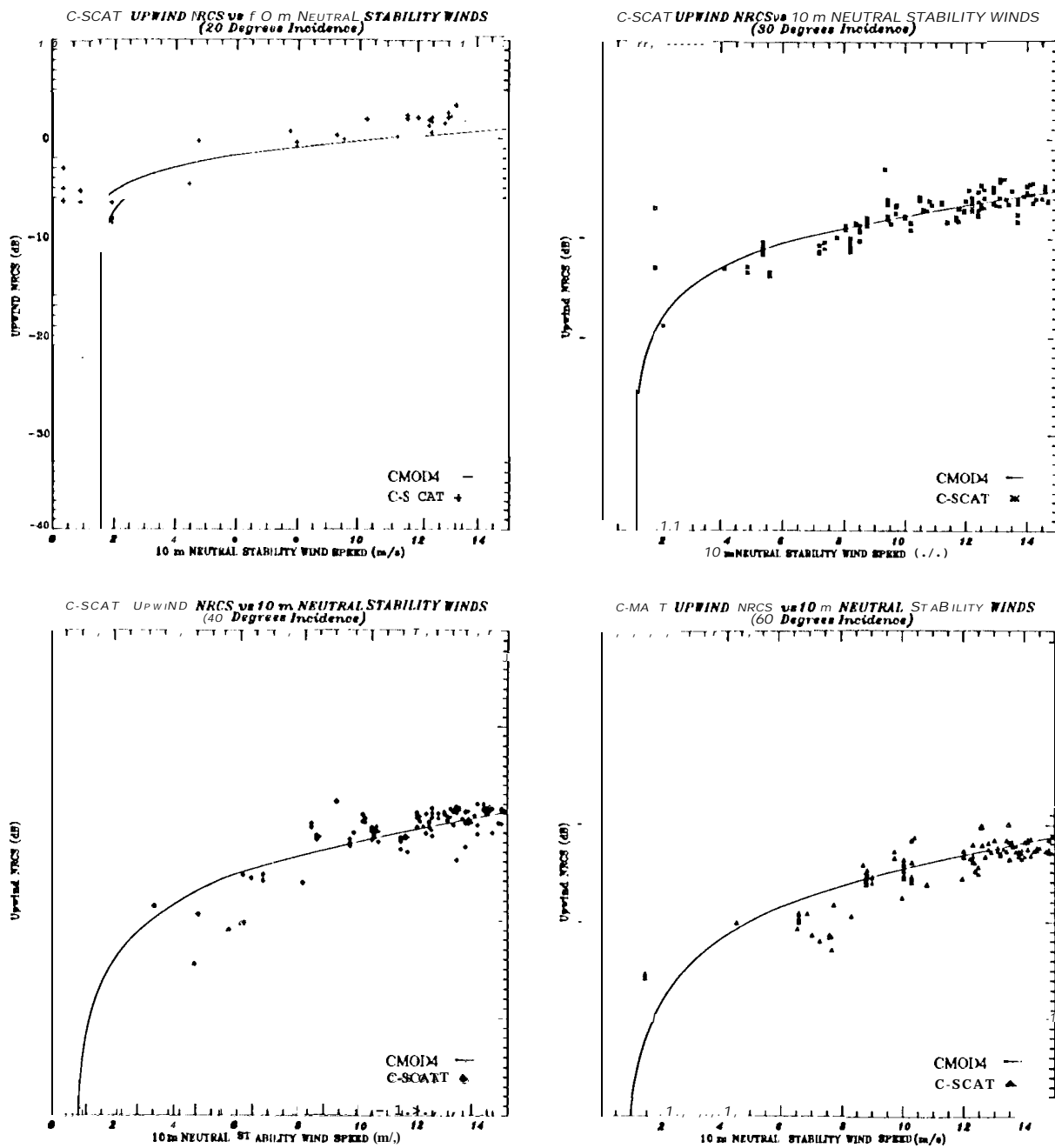


Fig. 18.

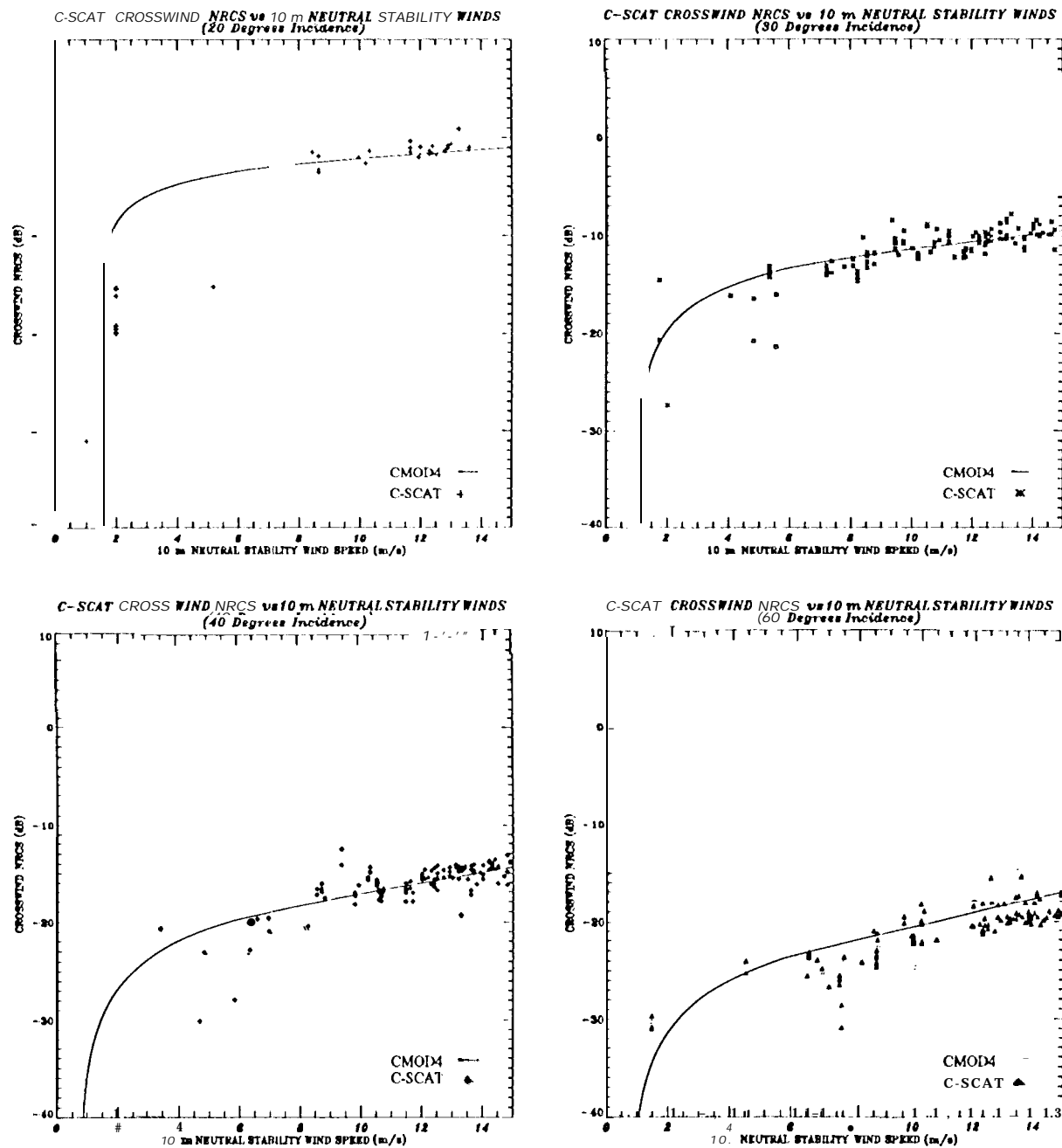
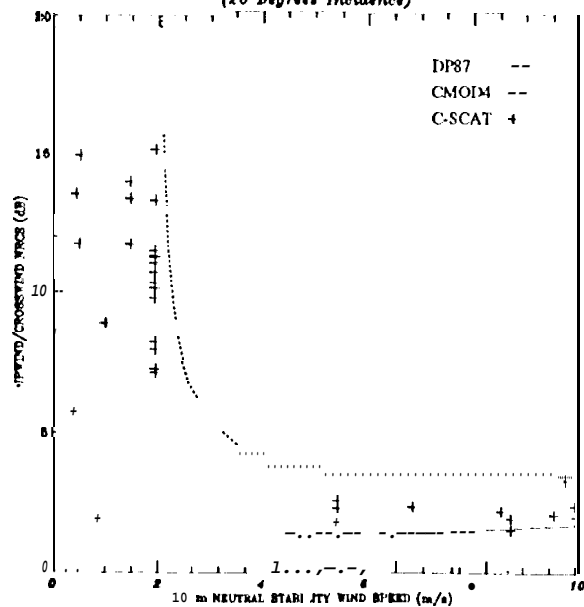
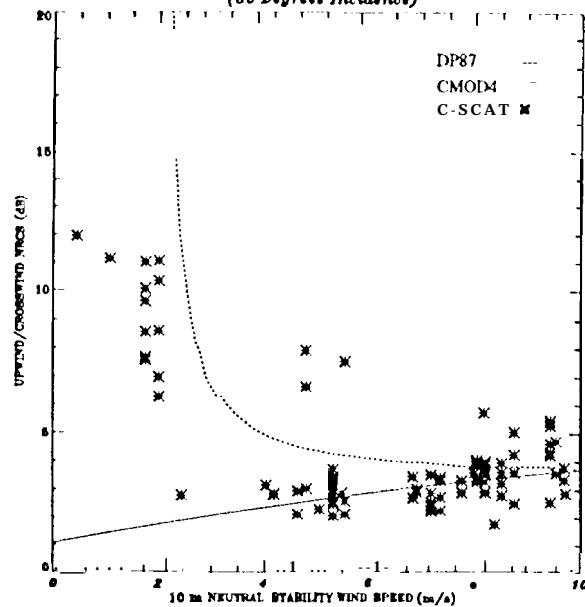


Fig. 19.

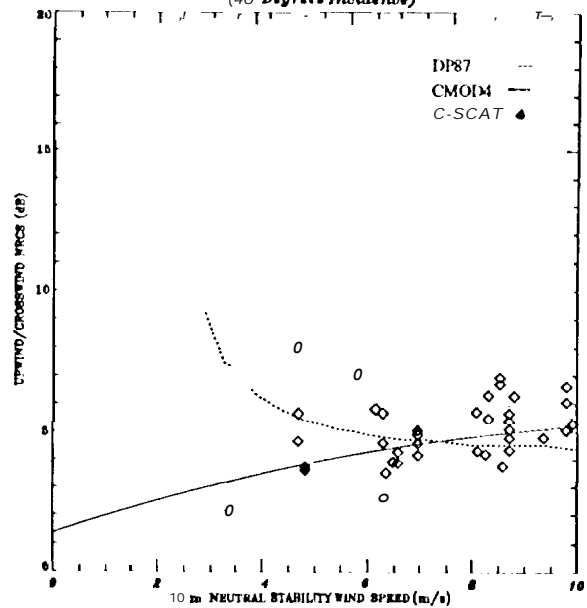
C-SCAT UPWIND/CROSSWIND NRCS vs 10 m NEUTRAL STABILITY WINDS
(20 Degree Incidence)



C-SCAT UPWIND/CROSSWIND NRCS vs 10 m NEUTRAL STABILITY WINDS
(30 Degree Incidence)



C-SCAT UPWIND/CROSSWIND NRCS vs 10 m NEUTRAL STABILITY WINDS
(40 Degree Incidence)



C-SCAT UPWIND/CROSSWIND NRCS vs 10 m NEUTRAL STABILITY WINDS
(60 Degree Incidence)

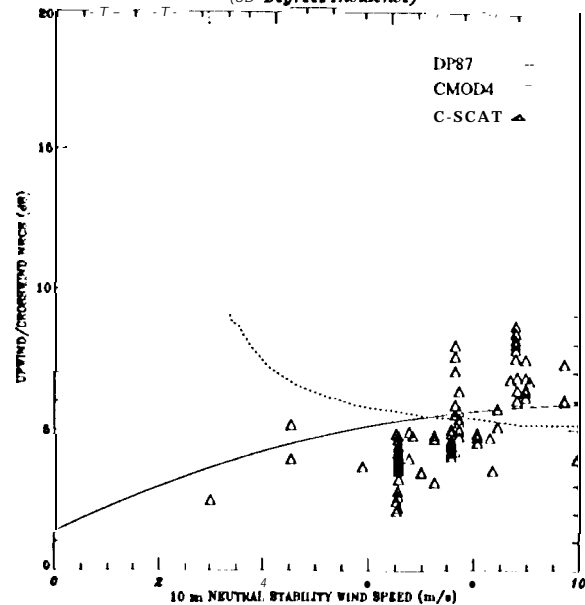
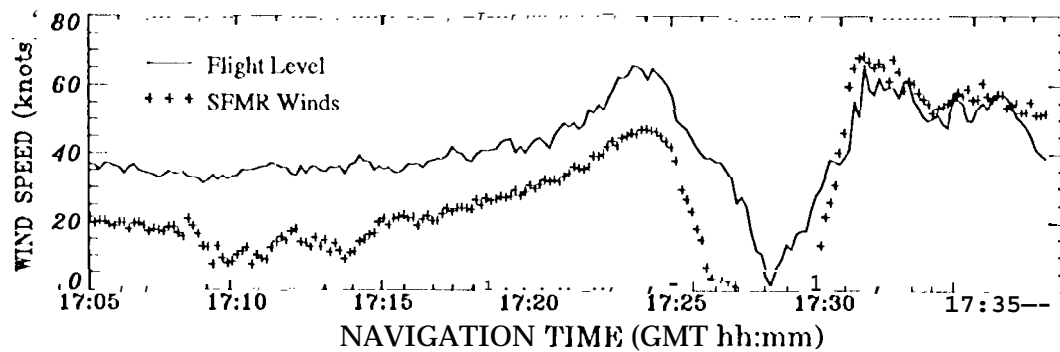
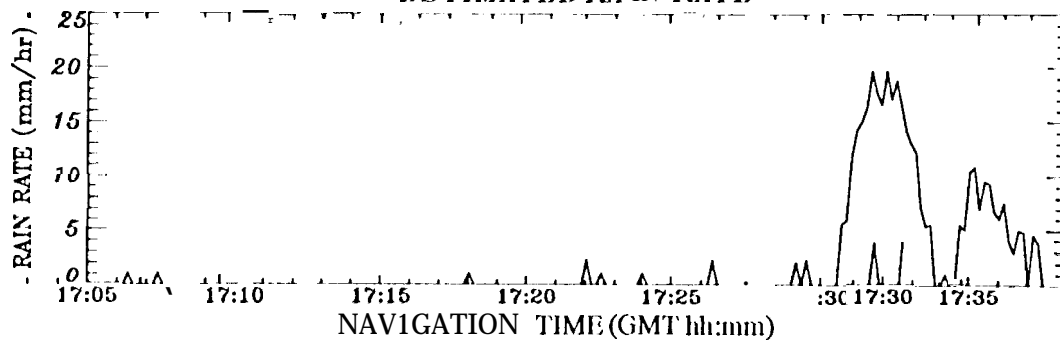


Fig. 20.

HURRICANE TINA: SEPT 21
MEASURED FLIGHT LA'VAL WIND SPEED



ESTIMATED RAIN RATE



RADIAL DISTANCE FROM HURRICANE CENTER

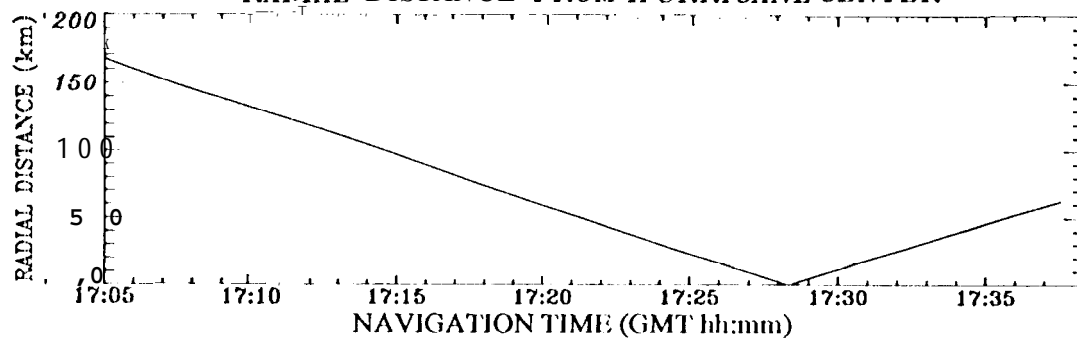


Fig. 21

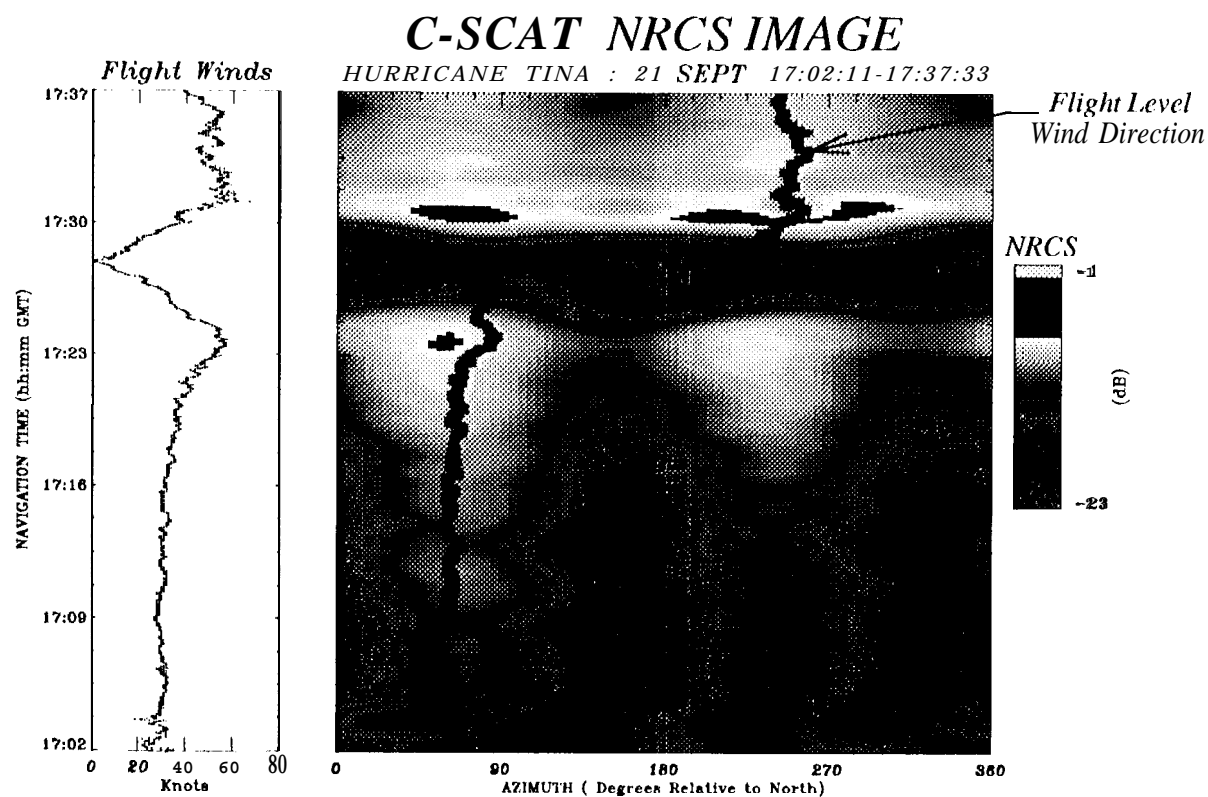


Fig. 22.

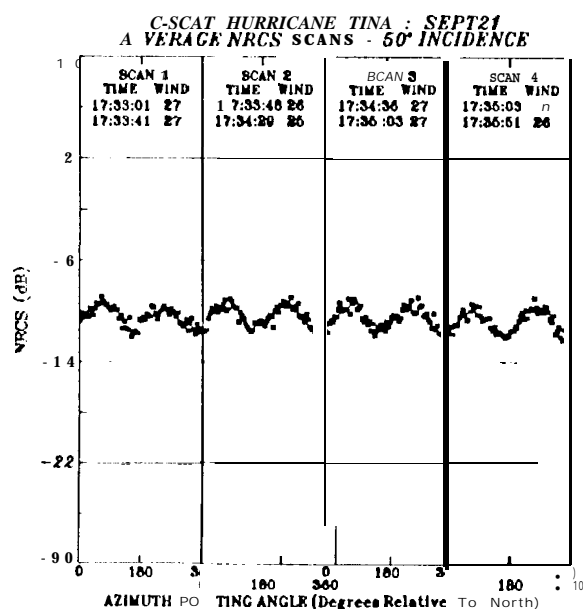
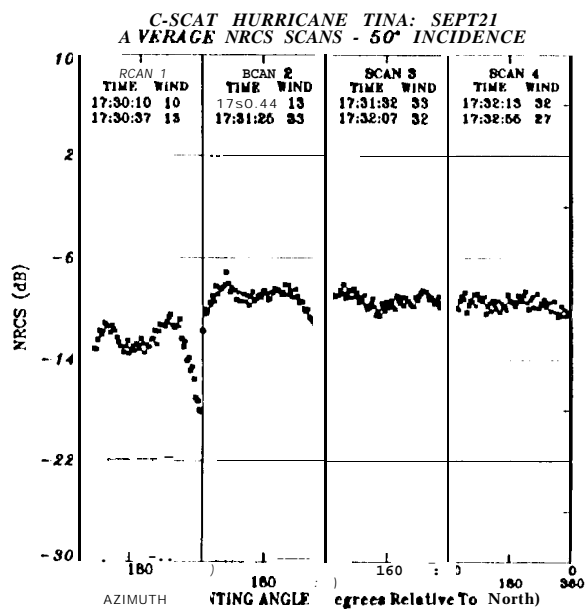
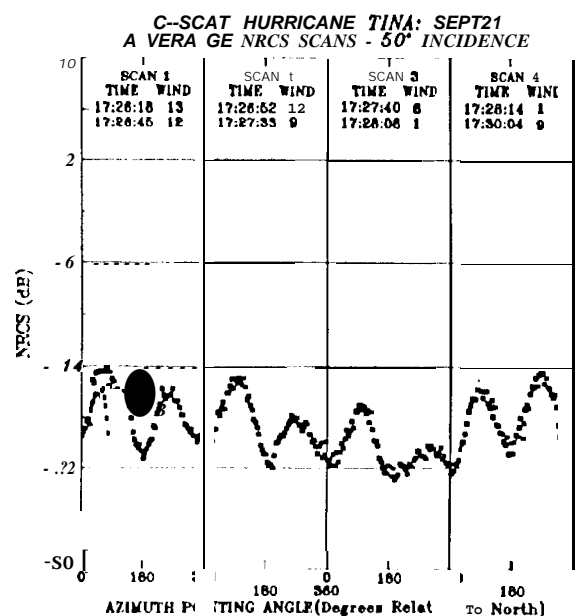
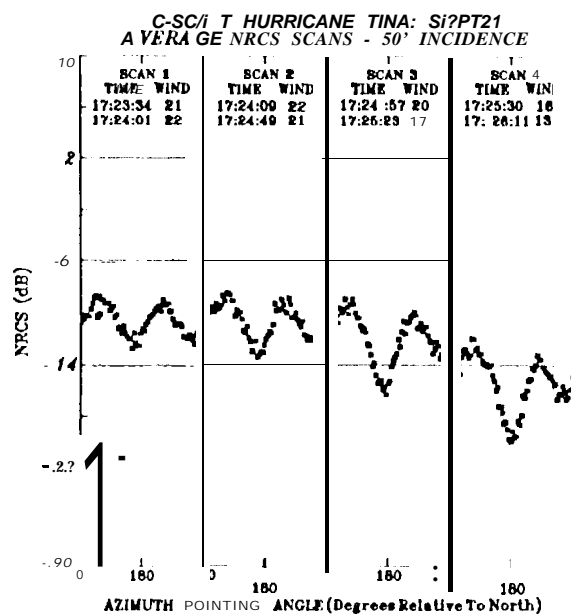


Fig. 24.

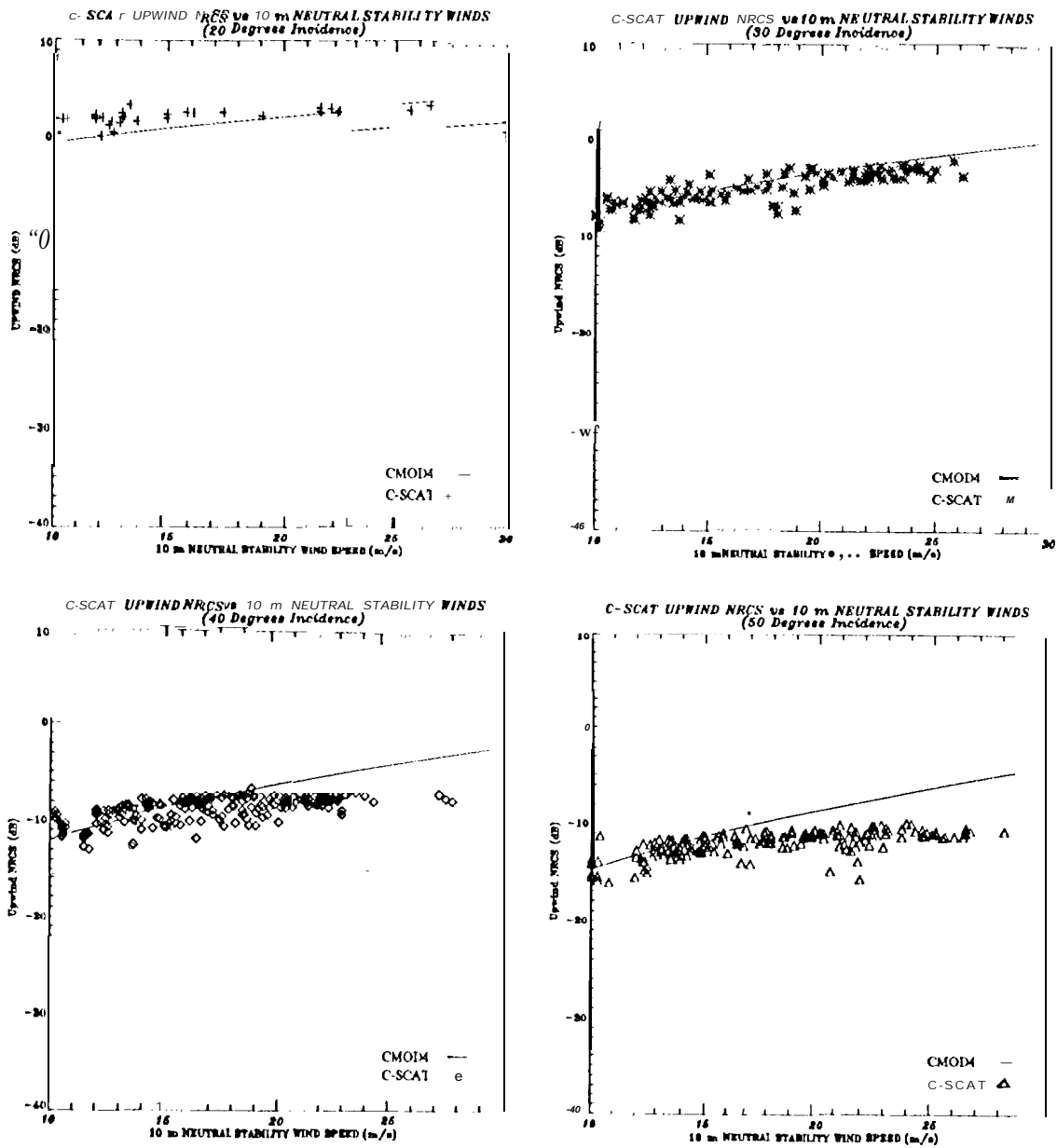


Fig. 25.

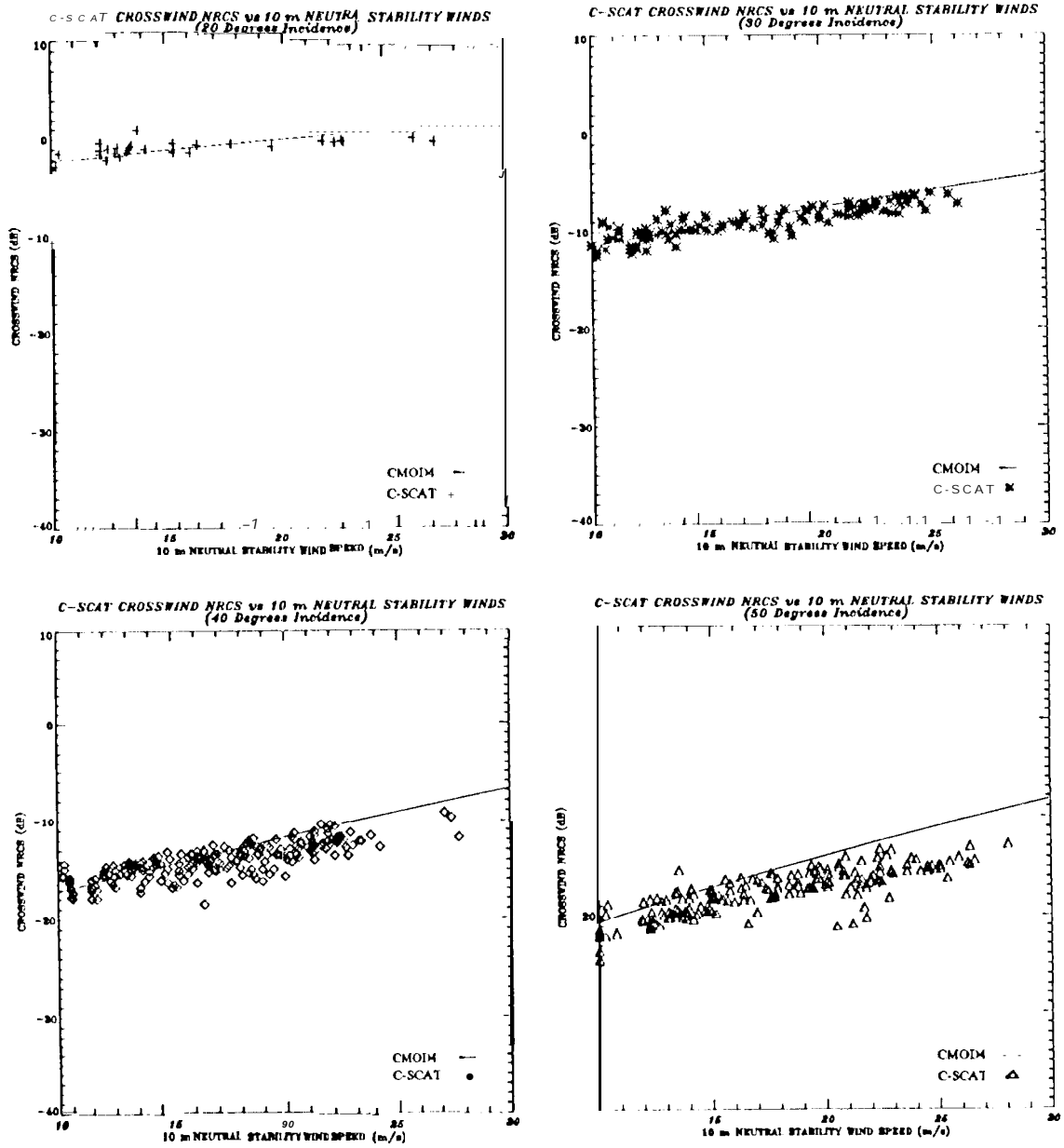


Fig. 26.

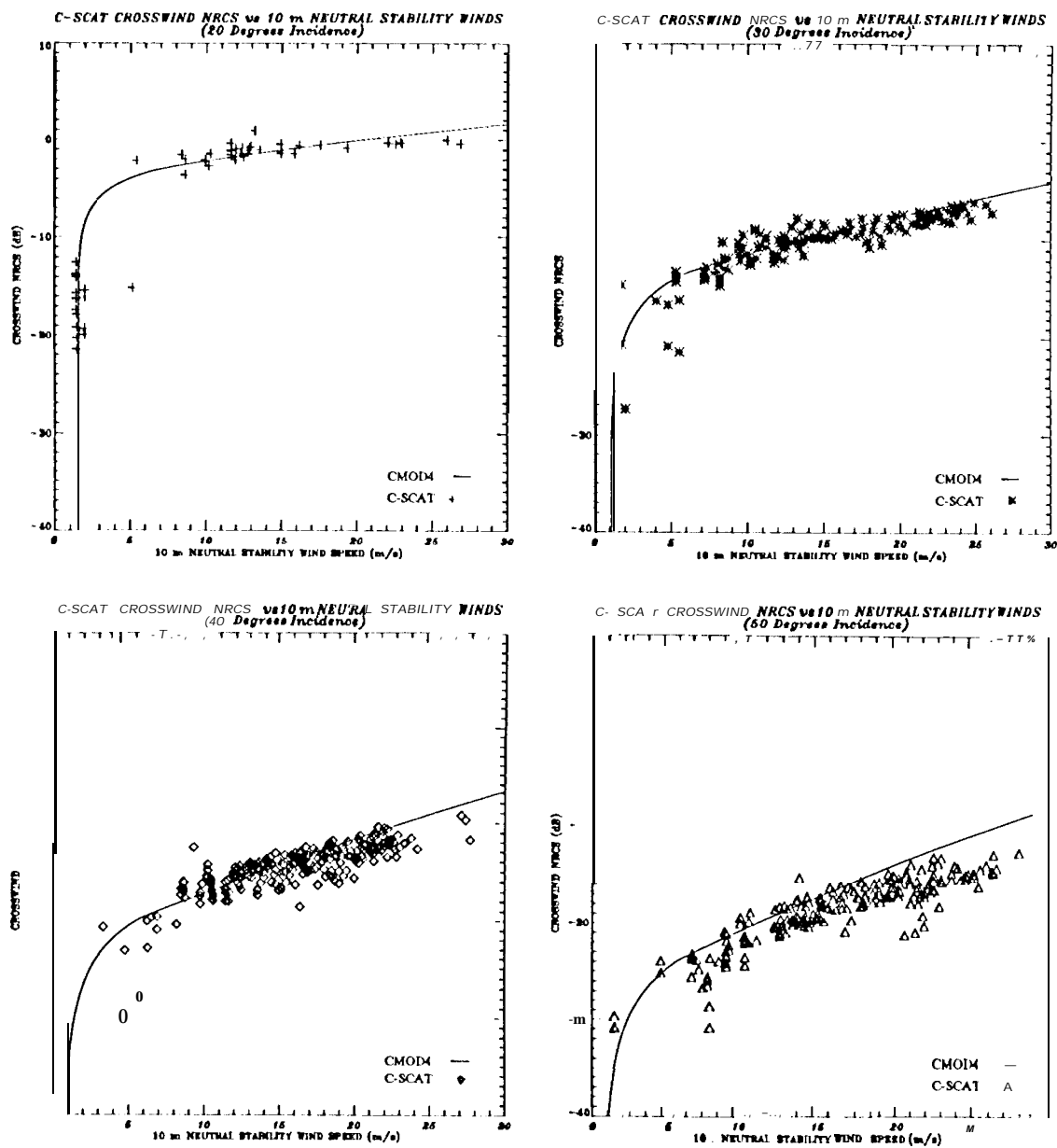


Fig. 28,

PARAMETER	NUSCAT	C-SCAT	C-SCAT]]	KU-SCAT
FREQUENCY (GHz)	13.900-13.995	4.97-5.70	4.98-5.70	12.8 -14.8
POLARIZATION	VV,HH,VH,HV	V v	V v	V v
INCIDENCE (degrees)	0 - 60	20-50	20-50	0-50
AZIMUTH (degrees)	0-360	0-360	0-360	0-360
SCAN RATE	10° step every 4 sees	0-30 rpm	0-100 rpm	0-100 rpm
PEAK POWER (watts)	10 or 250	.1 or 2	.1 or 5	.20r 10
ANTENNA GAIN (dB)	32	26.4 -29.1	26.4 -29.1	25-27-"
BEAM WIDTH (degrees)	4	4.2-6.3	4.2-6.3	4-6.3
PRF (KHz)	4-10	0.1-2	.1-30	.1-30
PULSE WIDTH (μsec)	15-75	.2-120	.2-120	.2-120
DETECTION	Square Law	Logarithmic	Logarithmic	Logarithmic

TABLE 1

INCIDENCE	NUSCAT	SASSI	C-SCAT	CMOD4
20°	-1.88	-1.77	-3.21	-1.76
30°	-1.88	-1.77	2.5	2.55
40°	-1.88	-1.77	1.90	2.34
50°	-1.88	-1.77	2.02	1.56

TABLE II